Ionospheric Correction of InSAR Time Series Analysis of C-band Sentinel-1 TOPS Data

Cunren Liang, Piyush Agram, Mark Simons and Eric J. Fielding

Abstract—The Copernicus Sentinel-1A/B satellites operating at C-band in TOPS mode bring unprecedented opportunities for measuring large-scale tectonic motions using interferometric synthetic aperture radar. However, while the ionospheric effects are only about one sixteenth of those at L-band, the measurement accuracy might still be degraded by long-wavelength signals due to the ionosphere. We implement the range split-spectrum method for correcting ionospheric effects in InSAR with C-band Sentinel-1 TOPS data. We perform InSAR time series analysis and evaluate these ionospheric effects using data acquired on both ascending (dusk-side of the Sentinel-1 dawn-dusk orbit) and descending (dawn-side) tracks over representative mid-latitude and low-latitude (geomagnetic latitude) areas. We find that the ionospheric effects are very strong for data acquired at low-latitudes on ascending tracks. For other cases, ionospheric effects are not strong or even negligible. Application of the range split-spectrum method, despite some implementation challenges, largely removes ionospheric effects and thus improves the InSAR time series analysis results.

Index Terms—Synthetic aperture radar interferometry (InSAR), ionosphere, range split-spectrum method, Sentinel-1, tectonic motion, time series analysis, TOPS.

I. INTRODUCTION

MEASUREMENTS of large-scale surface motion provides key constraints on our understanding of the Earth's tectonic processes. Such measurements are routinely made by global navigation satellite system (GNSS) at global scales with millimeter to centimeter-level precision and high temporal, but low spatial resolutions [1]. Recent development in spaceborne synthetic aperture radar (SAR) systems, in combination with SAR interferometry (InSAR) time series analysis techniques, provide observations with higher spatial resolution, but generally lower temporal resolution, limited coverage and larger uncertainties. The Copernicus Sentinel-1A/B satellites, launched in 2014 and 2016 and operated by the European Space Agency (ESA), opens new era for mapping large-scale tectonic motions. The satellites can operate up to 25 minutes per orbit [2] (orbital period: 98.6 minutes [3], [4]) with a wide swath of 250 km in its default TOPS mode [5], [6], and thus provide

large coverage. This two-satellite constellation and wide-swath mode reduce the repeat cycle to 6 days, a great improvement in temporal resolution compared to the 35-day repeat cycle of the previous ERS-1/2 and Envisat missions.

A major challenge for current repeat-pass InSAR techniques are the atmospheric effects. While tropospheric path delays in InSAR are almost independent of radar wavelength, ionospheric effects are typically considered to be small at the shorter-wavelength C-band. Considering a typical ratio of 4 between L-band and C-band wavelengths, the ionospheric effects including the InSAR light of sight (LOS) displacement error and azimuth pixel shift are only one sixteenth of those of L-band. However, ionospheric effects are still observed in C-band data. Such effects were seen in SAR data in polar areas [7], [8]. At C-band, since the fringes are mostly dominated by tropospheric signals, relatively small and slowly changing ionospheric signals are usually not clear in the interferograms. A large phase ramp found in one coseismic interferogram (160202-160214) of the 2016 Mw 6.4 Taiwan earthquake were among the first examples of clear ionospheric effects [9] in Sentinel-1 interferograms. More common examples in practical experience are found in the double-difference interferograms in the burst-overlap area after geometric coregistration, which sometimes have irregular patterns (e.g. [10], [11]).

Since the beginning of the 20th century, the Earth's ionosphere has been extensively studied in a number of relating fields such as radio communication, geomagnetism, space weather, atmospheric sciences and others. Of particular relevance to our study, global positioning system (GPS) satellites transmit L-band signals at two different frequencies L1 (1575.42 MHz) and L2 (1226.60 MHz) to make use of the dispersive nature of ionospheric effect on the propagation of radio waves for ionospheric corrections [1]. Recently this dispersive nature has been exploited for ionospheric corrections in InSAR measurements [12-14]. Because two radar frequencies are not directly available from past and current spaceborne SAR systems, the range radar spectrum is split into two subbands, each with a different center frequency and therefore it is called the range split-spectrum method (perhaps a better name should be dual-frequency/wavelength method). Subsequent developments [15-17] of this method, including implementations for data acquired in TOPS and ScanSAR modes [18], [19], show its potential for operationally removing ionospheric effects in InSAR. It is, however, still not very clear what ionospheric effects look like in most of the C-band TOPS interferograms, and most importantly how it affects

measurement of large-scale tectonic motion, which is the primary motivation for correcting long-wavelength signals caused by ionosphere at C-band. We implement the ionospheric correction for C-band TOPS InSAR data and present the correct results.

Our paper is organized as follows. Section II overviews spatial and temporal variations of the global ionosphere. Section III describes our implementation of the range split-spectrum method for C-band Sentinel-1 TOPS data, and the challenges and limitations of the method. We also describe problems and their solutions associated with the TOPS SLC products released by ESA. Section IV presents the ionospheric effects in InSAR time series analysis, and how ionospheric corrects can improve the results. Finally, Section V concludes the paper.

II. A BRIEF OVERVIEW OF THE SPATIAL AND TEMPORAL VARIATIONS OF THE GLOBAL IONOSPHERE

The Earth's ionosphere is defined as the part of Earth's atmosphere where ions and free electrons are present in quantities sufficient to affect the propagation of radio waves [20]. Ionization of the atmosphere occurs when photons of short wavelengths (mainly from solar ultraviolet and X-rays, with other minor contributions such as cosmic rays) are absorbed by atmospheric gases, with a portion of the energy used to eject an electron, converting a neutral atom or molecule to a pair of charged species including a negatively charged electron and a companion positive ion [21]. This process is called photoionization. Its reverse process is called recombination, *which may also involve other neutral atoms or molecules*. The ionosphere consists of three primary regions named by letters D (50~90 km), E (90~150 km) and F (150~1000 km). There is a remarkable anomaly of the E region called sporadic-E or Es, which is a transient and thin patch of enhanced electron density with a horizontal extent of 10~1000 km [22]. Typical vertical profiles of electron density in the mid-latitude ionosphere are shown in Fig. 1(a) [23]. Above the ionosphere is the magnetosphere where solar wind interacts with the Earth's geomagnetic field.

During the day, ionizing radiation from the Sun increases with height but the concentration of ionizable gas decreases with height, such that photoionization reaches a maximum at somewhere mid-ionosphere. In addition, photoionization also decreases with the solar zenith angle (defined such that the solar zenith angle is zero when the Sun is overhead). These basic principles of the photoionization production are encapsulated in Chapman theory. Note that the balance between electron production and loss involves not only photoionization and recombination, *but also many other physical processes*.

For radio wave propagation through the ionosphere, an important concept is the critical frequency. If the frequency of the radio wave is below critical frequency, a wave component is reflected by an ionospheric layer, making long distance radio communication possible despite of the Earth's curvature. If the frequency of the radio wave is above critical frequency, the wave penetrates through the ionospheric layer, which is what allows for spaceborne radar.

A. Spatial variations

Ionization of the atmosphere is mainly caused by the Sun, and therefore the intensity of ionization should generally decrease from geographic equator to the two geographic poles of the Earth. However, global ionization is also largely dominated by Earth's geomagnetic field. The geomagnetic field varies at time scales from seconds to millions of years. Currently its equator and poles are displaced from the geographic equator and poles by more than 10° [24]. The global distribution of electron density is generally aligned along the geomagnetic latitudes. The global ionosphere can be roughly divided into three regions according to their *geomagnetic latitudes*, including low-latitudes (0 ° ~20 °), mid-latitudes (20°~60°) and high-latitudes (60°~90°) [26]. These regions, as shown in Fig. 1(b), are overlaid on a global vertical TEC map interpolated from results processed by NASA JPL (https://iono.jpl.nasa.gov/) using data from International GNSS Service [27].

At mid-latitudes, the ionosphere is quietest with slow spatial variations, except during some rare events such as geomagnetic storms. At low-latitudes, ionization is highest because the sun is mostly overhead. On both sides of the geomagnetic equator, at geomagnetic latitudes about 10° to 15°, ionization reaches maximum. It is called Appleton or equatorial anomaly [28]. For InSAR applications, one typical area of such maximum ionization is northern Chile where strong ionospheric effects have been observed in many interferograms. Another well-known phenomena at low-latitudes are equatorial scintillations, typically observed as amplitude stripes in SAR images [29-31]. At high-latitudes, the ionosphere is connected, via the geomagnetic field, to the outer magnetosphere and the solar wind. Charged particles energized within the magnetosphere or from the Sun enter the ionosphere, becoming another main source of ionization [26], [32]. The many dynamic processes involved make the high-latitude ionosphere subject to the highest level of variations which cause artifacts even observable in C-band SAR data [7], [33]. Perhaps the most well-known natural phenomena at high-latitudes are aurora, which are a consequence of energetic particles entering the atmosphere from the magnetosphere. Between the mid-latitude and high-latitude near 60 ° ~65 ° geomagnetic latitude, there is a region of decreased ionization in the F region called the main trough. The ends of the trough are typically found an hour after sunset and an hour before sunrise [34]. It is also reportedly observed in SAR data [29].

B. Temporal variations

Ionization is mainly caused by the Sun, the intensity of ionization is related to the relative position between the Earth and the Sun, and the Sun's activities. As a result, ionosphere is subject to diurnal, seasonal and solar cycle variations. Overall, ionization is much stronger at daytime than at night. During night, free electrons in the D region almost totally disappear. While the E region remains at night, it is only weakly ionized. During the day, the F region splits into a lower layer, F1, and an

upper layer, F2. At night, they merge at about the level of the F2 layer with reduced ionization. Chapman theory is valid for lower layers including E region and F1 layer. The D region is not well modelled by Chapman theory due to the complex photochemical processes involved. The F2 layer has the greatest concentration of electrons among all the layers, but is also most variable, most anomalous and most unpredictable [32]. One of the anomalies of the F2 layer is that the daytime maximum electron density is greater in winter than in summer, opposite predictions from Chapman theory. However, the Sun does affect the electron density of the F2 layer, causing a rapid increase after sunrise [26].

Over the course of the approximately 11-year solar cycle, the intensity of ionizing solar radiation varies. The temperature of the upper atmosphere also varies with solar activity, leading to variations in the gas density [32]. Therefore, ionization is closely related to solar cycle. The solar cycle is linked to changes in the Sun's magnetic field, which completely flips every 11 years or so. A well-known indicator of the solar cycle is the rise and fall in the numbers of sunspots [35]. At solar minimum (least solar activity) in the cycle, there are the fewest sunspots, and ionization is lowest. At solar maximum (greatest solar activity), there are the most sunspots, and ionization is highest.

III. The Range Split-Spectrum Method for the InSAR Ionospheric Correction of C-band Sentinel-1 TOPS Mode

A. Background

The effect of the Earth's ionosphere on a traversing microwave signal can be described by the Appleton-Hartree equation, from which we can derive a phase shift and a Faraday rotation [36], [37]. Due to the phase shift, the two-way phase delay of the radar signal is [38]

$$\phi_{\text{ion}} = -\frac{4\pi K}{cf}\text{TEC} \qquad (1)$$

where $K=40.28$ m^3/s^2, c is the speed of light in vacuum, f is the frequency of the microwave signal, and TEC is the total electron content (TEC) along the radar signal traveling path. The phase delay is inversely proportional to the signal frequency, which is called dispersive nature. The C-band frequencies are about four times L-band frequencies, considering the typical radar wavelengths used by current SAR systems. Therefore, when the InSAR phase is converted to displacement, the error caused by ionosphere is only about one sixteenth of that of L-band. In our InSAR processing, we treat the ionosphere as a thin layer, although it has vertical structure and extends from about 50 km to 1000 km above the Earth.

By making use of the dispersive nature, the range split-spectrum method [12-14] for InSAR ionospheric correction creates a lower and upper band signals by bandpass filtering the range spectrum of the original radar signal. We then compute the ionospheric phase in the interferogram by

$$\Delta\phi_{\text{ion}} = \frac{f_l f_u}{f_0(f_u^2 - f_l^2)}(\Delta\phi_l f_u - \Delta\phi_u f_l) \qquad (2)$$

where f_0 is the center frequency of the original radar signal, f_l

and f_u are the center frequencies of the newly created lower and upper band signals, respectively, and $\Delta\phi_l$ and $\Delta\phi_u$ are the phases of the lower and upper band interferograms, respectively. Since the azimuth signal of a target is collected within a synthetic aperture, the azimuth resolution of the estimated ionospheric phase is thus determined by the synthetic aperture length projected onto the ionosphere layer, which reflects the low-pass signatures of the ionosphere. The range split-spectrum method has been proved to be an effective method for correcting the ionospheric phase in InSAR interferograms [15-19].

The linear change of the phase delay within the synthetic aperture of a target causes azimuth pixel shift of the focused target. For InSAR, the relative azimuth shift (on the ground) of the same target in the reference and repeat (previously known as master and slave) images can be calculated by [18]

$$\Delta x_{\text{ion}} = \frac{v_g}{K_a} \cdot \frac{1}{4\pi} \cdot \frac{\partial\Delta\phi_{\text{ion}}}{\partial\eta} \ [m] \qquad (3)$$

where v_g is the velocity of the radar beam footprint on the ground, K_a ($K_a < 0$) is the azimuth frequency modulation (FM) rate, and η is the azimuth time. At C-band, K_a is approximately four times that at L-band, but $\Delta\phi_{\text{ion}}$ is about one fourth of that at L-band. The azimuth shift at C-band is thus only about one sixteenth of that of L-band.

In TOPS mode [5], the radar images several subswaths using a burst technique. In each subwath, the burst is repeated cyclically, and during a gap between two adjacent bursts, the radar antenna is pointed to other subswaths. Within a burst, the antenna rotates from backward to forward in the azimuth direction such that each imaged target experiences the full azimuth antenna pattern. The Sentinel-1 TOPS mode is a single-look burst mode, whereby each target on the ground is imaged by only one burst, except in the small overlapping area between two adjacent bursts.

As far as the ionosphere is concerned, two effects should be noted because of the particular imaging mode. The first is that the azimuth position of the imaged ionosphere deviates from the azimuth position of the imaged target on the ground, and the deviation changes with azimuth across the burst. Consider a target in the burst overlap area as shown in Fig. 2. In burst n, its center Doppler frequency position η_{dc}^n, relative to its zero Doppler position η_{zd}, is

$$\begin{aligned}\eta_{\text{dc},\delta}^n &= \eta_{\text{dc}}^n - \eta_{\text{zd}} \\ &= (\eta_{\text{zd}} - \eta_{\text{bc}}^n)\frac{K_t}{K_a}\end{aligned} \qquad (4)$$

where η_{bc}^n is the position in the focused burst where the center Doppler frequency is zero, and K_t is the slope of the azimuth burst spectrum after focusing. The intersection of the radar light-of-sight (LOS) and the ionosphere layer η_{ion}^n, relative to the zero Doppler position, is

$$\begin{aligned}\eta_{\text{ion},\delta}^n &= \eta_{\text{ion}}^n - \eta_{\text{zd}} \\ &= (\eta_{\text{dc}}^n - \eta_{\text{zd}}) \cdot \frac{h_{\text{ion}}}{h_{\text{sat}}} \\ &= (\eta_{\text{zd}} - \eta_{\text{bc}}^n)\frac{K_t}{K_a} \cdot \frac{h_{\text{ion}}}{h_{\text{sat}}}\end{aligned} \qquad (5)$$

where h_{ion} and h_{sat} are the heights of the ionosphere layer and

the satellite, respectively. In the next burst $n+1$, the intersection becomes η_{ion}^{n+1} for the same target on the ground, leading to phase jumps on the burst edges in the mosaicked interferogram. These jumps or discontinuities should be properly handled in the ionospheric correction.

A second effect in the imaging is the linear change of the center Doppler frequency in the focused burst, and the center frequency can be very large on burst edge due to the rotation of the antenna. The large linear phase in the time domain corresponding to the large center Doppler frequency requires high precision coregistration, which is typically done by the so-called enhanced spectral diversity (ESD) [6], [39]. As discussed earlier, ionosphere can cause azimuth pixel shift. This shift, together with the large linear phase in the target due to its large center frequency, might lead to a large phase error in the interferogram, such as the phase jumps on burst edges in the mosaicked interferogram. The Sentinel-1 is a C-band SAR satellite, and the azimuth resolution of its TOPS mode is relatively coarse. The azimuth shift caused by ionosphere does not lead to significant decorrelation in most cases. If we know the relative azimuth shift of the InSAR pair, the resulting phase error can be computed and therefore compensated by

$$\Delta\phi_\epsilon = 2\pi f_c \frac{\Delta x_{\text{ion}}}{v_g} \tag{6}$$

where f_c is the center Doppler frequency.

B. Implementation

Our implementation of the range split-spectrum method for the InSAR ionospheric correction of Sentinel-1 TOPS mode starts after the coregistration step in the regular TOPS InSAR processing workflow. The coregistration step usually includes geometrical coregistration [40] and ESD [39], but for our ionospheric correction workflow, it does not matter whether ESD is included in coregistration or not. The main input includes the reference bursts, the repeat bursts, the coregistered repeat bursts, and the offsets between reference and repeat bursts. The output is the burst-level phase for correcting the interferograms. Throughout the entire ionospheric correction workflow, there is no interaction with the InSAR workflow. The ionospheric correction workflow is shown in Fig. 3.

Sentinel-1 has two TOPS modes including the Interferometric Wide Swath (IW) mode and the Extra Wide Swath (EW) mode. Our discussion below focuses on the most commonly used IW mode. The extension to the EW mode should be trivial. The workflow starts with range bandpass filtering. The range spectrum of the Sentinel-1 TOPS SLC product distributed by ESA is weighted by a Hamming window, probably to suppress the sidelobe of the focused target. Before range bandpass filtering, we remove this window. For each burst in the reference and repeat image products, we do bandpass filtering in range to create a lower and upper band bursts. The bandpass filtering process for a burst is shown in Fig. 4. At each subband, the burst interferograms are formed after resampling repeat bursts. Now we have two sets of subband interferograms.

The ionospheric phase might be very different in different bursts considering the imaging geometry of TOPS mode.

Therefore, the origin and indexes of each pixel in each burst must be accurately tracked in the entire workflow. No pixel in the mosaicked image should include pixels from different bursts after spatial averaging. For this purpose, we compute the indexes of the start and end pixels of the data chunk in each burst that eventually goes to the mosaicked image, considering the averaging window size. Normally there are more than 100 lines between two adjacent bursts within a subswath, and there are more than 600 samples between two adjacent subswaths. This should at least support 50(azimuth)×300(range) looks or a multiple-looked pixel size of 0.7 km (azimuth on ground) × 0.7 km (slant range), which is enough for most applications. In our processing, these indexes are not only used in the ionospheric correction workflow, but also used in the regular InSAR workflow.

With the burst start and end pixel indexes available, we can mosaic the bursts of all subswaths and take looks, and then we have two subband mosaicked interferograms. We unwrap the two interferograms using SNAPHU [41]. The ionospheric phase can then be computed by (2) using the two unwrapped interferograms.

As shown in Fig. 2, the computed ionospheric phase is actually the ionospheric phase from the ionosphere layer projected onto ground. We project the computed ionospheric phase onto the ionosphere layer by resampling the computed ionospheric phase considering the imaging geometry of TOPS mode. As a result, the burst shrinks in the azimuth direction. The result is shown in Fig. 5(a).

The ionospheric phase needs to be strongly smoothed in order to suppress noise. For this purpose, we use a Gaussian filter as in [15]. If we filter the resampled ionospheric phase directly, the number of samples available for filtering is reduced because of the shrinking. To avoid this, we can increase the sampling rate during resampling, or alternatively project the pixel index, instead of the ionospheric phase, onto the ionospheric layer. The pixel values remain the same, but the pixel indexes are changed. The pixel interval is not constant any longer, which reflects the distance on the ionosphere layer. In the filtering, the ionospheric phase before resampling and the changed pixel index are used. This, however, requires some changes to the filter implementation which usually assumes a constant pixel interval. In our implementation, we find that the filtering window size needs to be much larger than the azimuth burst size in order to get a reasonably smooth result. Therefore, we can just ignore the shrinking from ground to ionosphere layer and use the ionospheric phase before resampling directly. The filtering result is shown in Fig. 5(b). After filtering, we project the ionospheric phase back to the ground. The result is the burst-level ionospheric phase.

We also use the filtered ionospheric phase to compute the relative azimuth shift caused by ionosphere according to (3). The result is shown in Fig. 5(c). The introduced InSAR phase error by the relative azimuth shift can then be computed by (6). Again, the result is the burst-level phase.

With the burst-level ionospheric phase and phase error caused by relative azimuth shift available, we add them together. Note that at this stage, there might be residual azimuth

offset between reference and repeat images, so ESD, with ionospheric phase and phase error removed from the burst interferograms, is used to estimate this residual offset. Since ESD is done here, it does not matter whether the input offset from regular InSAR processing includes ESD offset or not. We then compute the InSAR phase error caused by this residual azimuth offset. Finally, we add the ionospheric phase, the phase error caused by relative azimuth shift, and the phase error caused by the residual azimuth offset together. The output is then burst-level phase for doing correction. The mosaicked burst-level phase is shown in Fig. 5(d). The interferograms before and after ionospheric correction are shown in Fig. 5(e) and (f), respectively. Note that, at C-band, the interferogram after ionospheric correction does not look as clean as that at L-band, because the same troposphere causes more fringes in the interferogram at C-band due to its shorter wavelength.

In this workflow, we don't consider the physical azimuth offset on ground, which affects the final ESD step.

C. Phase discontinuities in the burst overlap areas caused by ionosphere

Due to the imaging geometry of the TOPS mode, the ionospheric phase at η_{zd} in burst n becomes the ionospheric phase at η_{ion}^n (Fig. 2). Following (5), the change of the ionospheric phase at η_{zd} can be approximated by

$$\phi_{height,\delta}^n = \phi_{ion}(\eta_{ion}^n) - \phi_{ion}(\eta_{zd})$$
$$= \eta_{ion,\delta}^n \left.\frac{\partial \phi_{ion}}{\partial \eta}\right|_{\eta=\eta_{zd}} \tag{7}$$

where ϕ_{ion} is the ionospheric phase. If we assume ϕ_{ion} linearly changes in the azimuth direction, then the phase change is

$$\phi_{height,\delta}^n = \eta_{ion,\delta}^n K_{ion}$$
$$= (\eta_{zd} - \eta_{bc}^n)\frac{K_t}{K_a} \cdot \frac{h_{ion}}{h_{sat}} \cdot K_{ion} \tag{8}$$

where K_{ion} is the linear azimuth change rate of the ionospheric phase. If $K_{ion} > 0$, then $\phi_{height,\delta}^n < 0$, which implies that the ionospheric phase at η_{zd} becomes smaller. The phase change reaches maximum at burst edges. Note that this is the phase change of *one* acquisition. The result of the other acquisition of the InSAR pair is of the same form, but with different h_{ion} and K_{ion} values. Here and in the following discussions, we focus on the analysis of one acquisition.

The linear component of the ionospheric phase ϕ_{ion} results in an azimuth pixel shift in the focused image. To examine how it changes phase, we start from the phase of the original azimuth radar signal which is approximately a linear frequency-modulated (FM) signal

$$\phi_{raw} = \pi K_a (\eta - \eta_{zd})^2 \tag{9}$$

If a linear ionospheric phase $\phi_{ion} = K_{ion}\eta$ is added to this signal, we find

$$\phi_{raw+ion} = \pi K_a (\eta - \eta_{zd})^2 + K_{ion}\eta$$
$$= \pi K_a \left[\eta^2 - 2\left(\eta_{zd} - \frac{K_{ion}}{2\pi K_a}\right)\eta + \eta_{zd}^2\right] \tag{10}$$

The center of the signal is moved by $-K_{ion}/2\pi K_a$. After azimuth focusing, the focused target is moved by $-K_{ion}/4\pi K_a$, where we have considered the two-way radar signal. If $K_{ion} >$

0, then both the signal center and the focused target are moved to right. The phase change is mainly caused by the linear phase of the focused target and is

$$\phi_{azshift,\delta}^n = \phi\left(\eta + \frac{K_{ion}}{4\pi K_a}\right) - \phi(\eta)$$
$$= 2\pi f_c \left(\eta + \frac{K_{ion}}{4\pi K_a}\right) - 2\pi f_c \eta$$
$$= 2\pi f_c \cdot \frac{K_{ion}}{4\pi K_a} \tag{11}$$
$$= 2\pi(\eta_{zd} - \eta_{bc}^n)K_t \cdot \frac{K_{ion}}{4\pi K_a}$$
$$= \frac{1}{2}(\eta_{zd} - \eta_{bc}^n)\frac{K_t}{K_a} \cdot K_{ion}$$

where f_c is the center Doppler frequency. If $K_{ion} > 0$, then $\phi_{azshift,\delta}^n < 0$.

We can see that both $\phi_{height,\delta}^n$ and $\phi_{azshift,\delta}^n$ change linearly in the azimuth direction *with the same sign*. The InSAR phase error caused by a constant azimuth offset between the InSAR pair is also linear in the azimuth direction. Thus, both $\phi_{height,\delta}^n$ and $\phi_{azshift,\delta}^n$ can be treated as the InSAR phase error caused by a constant azimuth offset in ESD. In the overlap area of burst n and $n+1$, they cause a phase discontinuity

$$\phi_{ESD} = \phi_{height,\delta}^{n+1} + \phi_{azshift,\delta}^{n+1} + \phi_{ion}(\eta_{zd})$$
$$\qquad - [\phi_{height,\delta}^n + \phi_{azshift,\delta}^n + \phi_{ion}(\eta_{zd})]$$
$$= \phi_{height,\delta}^{n+1} - \phi_{height,\delta}^n + \phi_{azshift,\delta}^{n+1} - \phi_{azshift,\delta}^n$$
$$= [(\eta_{zd} - \eta_{bc}^{n+1}) - (\eta_{zd} - \eta_{bc}^n)]$$
$$\qquad \cdot \left(\frac{K_t}{K_a} \cdot \frac{h_{ion}}{h_{sat}} \cdot K_{ion} + \frac{1}{2}\frac{K_t}{K_a} \cdot K_{ion}\right) \tag{12}$$
$$= -T_C \frac{K_t}{K_a} \cdot \left(\frac{h_{ion}}{h_{sat}} + \frac{1}{2}\right) \cdot K_{ion}$$

If this phase is involved in ESD, the equivalent azimuth offset is

$$\eta_{ESD} = \frac{\phi_{ESD}}{2\pi\Delta f}$$
$$= -T_C \frac{K_t}{K_a} \cdot \left(\frac{h_{ion}}{h_{sat}} + \frac{1}{2}\right) \cdot K_{ion} \cdot \frac{1}{2\pi T_C K_t} \tag{13}$$
$$= -\frac{1}{2\pi} \cdot \frac{K_{ion}}{K_a} \cdot \left(\frac{h_{ion}}{h_{sat}} + \frac{1}{2}\right)$$

After ESD, $\phi_{height,\delta}^n$ and $\phi_{azshift,\delta}^n$ can be removed from the burst interferogram by either adding η_{ESD} to the coregistration offset or multiplying the burst interferogram with a linear phase. Therefore, when the ionospheric phase is mostly linear in the azimuth direction, the ionospheric phase in the mosaicked interferogram with ESD applied is like the ionospheric phase in a stripmap interferogram, which is a phase ramp without phase discontinuities in the burst overlap areas. In this case, a much larger offset estimated by ESD may be observed.

We compute the phase discontinuity and the equivalent azimuth offset using Sentinel-1 parameters at the center of middle subswath (Figs. 6(a) and (b)). We find that the phase discontinuity is usually smaller than 2π, which is true even in areas like Chile where ionospheric effects are nearly maximal. This is the reason why we can mosaic the burst interferograms

before phase unwrapping in our workflow of ionospheric correction as shown in Fig. 3. The azimuth pixel shift is also much smaller than the azimuth pixel size (azimuth pixel size on ground: 14.1 m), and therefore the resulting decorrelation can be ignored.

We use the height of the ionosphere layer in the calculation of ionospheric phase, but unfortunately this height is not known and so we use an empirical constant height. There are two steps that are impacted by the choice of the height of the ionosphere layer in the workflow shown in Fig. 3. The first step is the projection of the computed ionospheric phase from ground to the ionosphere layer before filtering. The second step is the reverse projection after filtering. We ignore the ionospheric phase error caused by the height error of the ionosphere layer in the first step, as its impact is small given the subsequent filtering with a large window size.

If there is an error $h_{\text{ion},\epsilon}$ in the ionosphere layer height h_{ion}, then the resulting error in $\eta_{\text{ion},\delta}^n$ in (5) is

$$\eta_{\text{ion},\epsilon}^n = (\eta_{\text{zd}} - \eta_{\text{bc}}^n)\frac{K_t}{K_a} \cdot \frac{h_{\text{ion},\epsilon}}{h_{\text{sat}}} \qquad (14)$$

After resampling the ionospheric phase from its original position η_{ion}^n to the zero Doppler position η_{zd} as shown in Fig. 2, we can approximate the introduced phase error by

$$\begin{aligned}\phi_{\text{ion},\epsilon}^n &= \eta_{\text{ion},\epsilon}^n \left.\frac{\partial \phi_{\text{ion}}}{\partial \eta}\right|_{\eta=\eta_{\text{zd}}} \\ &= \eta_{\text{ion},\epsilon}^n K_{\text{ion}} \qquad (15) \\ &= (\eta_{\text{zd}} - \eta_{\text{bc}}^n)\frac{K_t}{K_a} \cdot \frac{h_{\text{ion},\epsilon}}{h_{\text{sat}}} \cdot K_{\text{ion}}\end{aligned}$$

Here, we have also assumed the ionospheric phase ϕ_{ion} changes linearly in the azimuth direction. $\phi_{\text{ion},\epsilon}^n$ is also of linear form, which means it can also be treated as a phase error caused by a constant azimuth offset in ESD. Therefore, the final ESD offset estimate in our workflow (Fig. 3) also includes $\phi_{\text{ion},\epsilon}^n$.

So far, we have discussed the case of one acquisition. If InSAR phase is reference image phase minus repeat image phase, then the signs of $\phi_{\text{height},\delta}^n$, $\phi_{\text{azshift},\delta}^n$, ϕ_{ESD}, η_{ESD} and $\phi_{\text{ion},\epsilon}^n$ of reference image are changed. We have also ignored the azimuth frequency change of the target caused by the linear ionospheric phase, but this frequency change is small. Even if $K_{\text{ion}} = 1$ fringes/burst, the frequency change is only $K_{\text{ion}}/2\pi = 0.36$ Hz.

As the phase changes including $\phi_{\text{height},\delta}^n$ and $\phi_{\text{azshift},\delta}^n$ are linear in the azimuth direction, which is mostly true as ionosphere mostly slowly changes in space, the following simplified ionospheric correction workflow can serve as an alternative: (1) Remove continuous ionospheric phase (such as the filtered ionospheric phase in Fig. 3) from the burst interferograms, leaving only the phase changes ($\phi_{\text{height},\delta}^n$ and $\phi_{\text{azshift},\delta}^n$) in the burst interferograms. (2) Apply ESD at each burst overlap to estimate the offset, and low-pass filter, instead of taking average of, the resulting offsets to reduce noise caused by decorrelation. The offsets account for contributions from $\phi_{\text{height},\delta}^n$ and $\phi_{\text{azshift},\delta}^n$, errors associated with the satellite instruments such as orbit error, data processing error etc. (3) Add the offsets to coregistration offset, or multiply the burst interferograms with the equivalent phase ramps.

D. High frequency ionospheric effects

In the previous section (II-C), we have assumed constant h_{ion}, $h_{\text{ion},\epsilon}$ and K_{ion}. In practice, these parameters may change over the image. In addition, their values may be different between reference and repeat images. In the workflow for ionospheric correction, the ionospheric phase and the azimuth offset are smoothed, which also leads to errors. As a result, we cannot perfectly estimate the ionospheric phase screen, especially at small spatial scales. Fortunately, the ionospheric phase is smooth in most cases, and therefore the residual phase errors in the interferogram after correction are small.

When the ionosphere changes quickly over the imaged area, we cannot estimate the ionospheric phase screen well. Fig. 7 shows an example covering Mexico City, Mexico. After ionospheric correction, there is still high frequency ionospheric phase in the interferogram. In addition, we find remaining phase discontinuities in the burst overlap areas.

E. Pairs with different starting ranges

As radar flies along its track, it changes the slant range time for starting receiving echo (hereafter referred to as starting range) every short period of time. A long track of data is usually divided into a number of slices (or frame). After focusing, the starting range is usually the same for one or multiple SLC slices. In Sentinel-1 IW mode, there are three subswaths, each of which has a starting range. For multiple SLC slices of one acquisition, we find that starting ranges are occasionally different such as in the case of multiple SLC slices focused by different versions of the Sentinel-1 IPF software. For the same track and same area, the starting ranges of the SLC slices of different acquisition dates are usually the same, but sometimes are different. There is a much higher chance of different starting ranges among the early Sentinel-1A SLC slices acquired at different dates. These slices are floating along the track and not fixed. For the recent Sentinel-1A acquisitions, especially Sentinel-1B acquisitions, the chance is much lower. These slices are mostly fixed.

In the computed ionospheric phase, sometimes there is a discontinuity between two adjacent subswaths (Fig. 8(a)). The discontinuity is likely caused by the starting range errors of the reference and repeat SLC slices. The starting range error of an SLC slice has contributions from SAR instrument error, which is also present in the raw data, and errors in focusing. For each subband of reference or repeat SLC, if there is a relative starting range error $\Delta\tau_{0,\epsilon}$ between two subswaths, it causes a relative phase error between the two subswath interferograms, which eventually propagates to the computed ionospheric phase [18]. However, if reference and repeat SLCs have the same starting range error, their resulting phase errors in the subband interferogram cancel out, and therefore there is no phase discontinuity in the computed ionospheric phase. We find that when reference and repeat starting ranges are different, there is a very high probability of observing discontinuity between adjacent subswaths in the computed ionospheric phase; on the other hand, there is no such discontinuity if reference and repeat

starting ranges are the same. The starting range error caused by the instrument is probably stable. It is likely that, due to the problem of the focusing program, when the slice is focused with a different starting range, the resulting starting range error is also different. Therefore, if the ionospheric phase is computed using reference and repeat SLCs with different starting ranges, the starting range errors of reference and repeat SLCs are different and there will be discontinuities between adjacent subswaths.

One method of removing the discontinuity in the computed ionospheric phase is do the correction on the interferogram level, that is, computing the mean phase difference of the two adjacent subswath interferograms in the overlap area, removing the relative phase error from the interferograms, and then using the corrected interferograms to compute ionospheric phase [18]. For TOPS mode, however, $\phi_{\text{height},\delta}^n$ and $\phi_{\text{azshift},\delta}^n$ of the two adjacent subswath interferograms are different. To minimize their impacts, we do the correction on the computed ionospheric phase level. The workflow is shown on the right side of Fig. 3. We first compute the ionospheric phase of each subswath individually. We then compute the mean difference of the subswath ionospheric phases in the overlap area, and remove the difference. The subswath ionospheric phases can now be mosaicked. This avoids the effect of $\phi_{\text{azshift},\delta}^n$. The resulting mosaicked and filtered ionospheric phases are shown in Fig. 8(b) and (c), respectively. If the subswath ionospheric phases are projected from the ground onto the ionosphere layer before computing the mean difference, we can also reduce the effect of $\phi_{\text{height},\delta}^n$, and its residual error depends on the error in the ionosphere layer height used to do the projection. Oversampling can be considered to avoid reducing the number of samples in the projection.

In addition to the discontinuities in the computed ionospheric phase between subswaths, there are also discontinuities within one subswath as seen in Fig. 8(a). A possible explanation for these discontinuities is the different range errors as a result of doing range focusing and range cell migration correction range-chunk by range-chuck, as the number of range samples is large. This discontinuity also affects the computed mean difference of the subswath ionospheric phases in the overlap area, but we are not able to quantify it. For the filtering of the ionospheric phase, this discontinuity is small compared to the filtering window size, so it does not seem to affect the filtered phase very much.

Another error in the computed mean difference of the subswath ionospheric phases in the overlap area is from decorrelation. In each acquisition, the same target in the subswath overlap area is imaged by two bursts of the two subswaths. The Doppler spectra of the target in the two bursts do not overlap, because the two bursts are acquired at different orbit locations. Therefore, the phases of the two burst interferograms are statistically independent. The computed ionospheric phases of the two subswaths are also independent. When we compute their difference, their noises due to decorrelation do not cancel out.

To estimate the error due to decorrelation, we start from the phase standard deviation of a spatially averaged interferogram [42]

$$\sigma_{\Delta\phi} = \frac{1}{\sqrt{2N}} \frac{\sqrt{1-\gamma^2}}{\gamma} \tag{16}$$

where γ is the coherence, and N ($N > 10$) is the number of resolution elements. When using the range split-spectrum method to compute the ionospheric phase, the lower and upper range bands usually do not overlap, and therefore the phases of the lower and upper band interferograms are independent. Thus, the standard deviation of the computed ionospheric phase can be given by

$$\sigma_{\Delta\phi_{\text{ion}}} = \frac{f_l f_u}{f_0(f_u^2 - f_l^2)} \sqrt{f_u^2 \sigma_{\Delta\phi_l}^2 + f_l^2 \sigma_{\Delta\phi_u}^2} \tag{17}$$

where $\sigma_{\Delta\phi_l}$ and $\sigma_{\Delta\phi_u}$ are the phase standard deviations of the lower and upper band interferograms, respectively. The standard deviation of the difference of the two subswath ionospheric phases can be given by

$$\sigma_{\Delta\phi_{\text{ion}}^{s,s+1}} = \sqrt{\sigma_{\Delta\phi_{\text{ion}}^s}^2 + \sigma_{\Delta\phi_{\text{ion}}^{s+1}}^2} \tag{18}$$

where $\sigma_{\Delta\phi_{\text{ion}}^s}$ and $\sigma_{\Delta\phi_{\text{ion}}^{s+1}}$ are the standard deviations of the two subswath ionospheric phases, respectively. We assume the coherences of all samples in the overlap area are the same, and the standard deviation of the mean subswath ionospheric phase difference of one slice as a result of decorrelation is shown in Fig. 9.

To evaluate the performance of using the computed mean difference of the subswath ionospheric phases in the overlap area to remove the subswath discontinuities, we compute the ionospheric phase using both workflows shown in Fig. 3 and compare the results. We do this for many pairs with same starting ranges in our experimental areas discussed in Section III. We find that the error of the computed mean difference is usually smaller than 0.5 rad. Although the result of a specific pair depends on its coherence, the number of bursts in the pair, and so on, this provides an idea about the precision of the computed mean difference.

F. Cross Sentinel-1A/B pairs

For cross Sentinel-1A/B pairs, we find there is a small additional range ramp in the computed ionospheric phase. To extract this range ramp, we find an InSAR pair with very small ionospheric phase as shown in Fig. 10(a). We average the computed ionospheric phase over each column and fit a polynomial to the mean phase as shown in Fig. 11. The resulting polynomial is

$$\Delta\phi_{\text{ion,ramp}} = 1.05 - 4.56r + 2.96r^2 + 0.95r^3 \tag{19}$$

where r ($0 \le r \le 1$) is the scaled range. The range ramp computed from this polynomial is shown in Fig. 10(b). We then remove the computed ramp from the ionospheric phase shown in Fig. 10(a), and get the result shown in Fig. 10(c).

Note that this is the ramp for descending S1A-S1B pair. For ascending pair, it should be flipped in the range direction. Furthermore, for S1B-S1A pair, the sign of the ramp should be changed. We find this empirical ramp also applies to other pairs we processed over western United States and northern Chile. More pairs should be processed in the future for testing its

global applicability.

G. Relative azimuth FM rate error

The azimuth FM rate usually cannot be accurately computed in focusing due to the varying topography and other reasons. If the azimuth FM rate errors of reference burst and repeat burst are different, they result in a phase error in the burst interferogram. This happens when reference and repeat images are focused by different versions of the ESA Sentinel-1 IPF software and the two versions of IPF use different terrain heights to compute azimuth FM rates used in focusing. This phase error can be very large in high mountain areas, which is another cause of the discontinuities between adjacent burst interferograms. In such case, we correct this error using the method in [43], in addition to ionospheric correction. A joint correction example is shown in Fig. 12.

H. Decorrelation and phase unwrapping errors

As in L-band and stripmap cases, decorrelation and phase unwrapping errors are the two main problems affecting the performance of the range split-spectrum method for C-band TOPS data. In general, compared with L-band missions such as ALOS-2, decorrelation is a more critical issue at C-band, and there is a higher chance of phase unwrapping errors.

The radius of the Sentinel-1 orbital tube is about 100 m [44]. The small baseline results in small relative range spectral shift between reference and repeat images [45], and therefore results in small loss of the range resolution of the interferogram. More importantly, the small baseline helps reduce the volume decorrelation [46-49]. Overall, the resolution (range×azimuth) and the incidence angle are about the same as those of previous missions such as Envisat, so we don't expect a big change of volume decorrelation associated with resolution and incidence angle. The temporal decorrelation is much reduced because of the short repeat cycle of 6 or 12 days. However, data are not always acquired on such regular basis. Despite the reduced volume decorrelation and temporal decorrelation, we find that decorrelation is still a major problem that has significant impact on the performance of the range split-spectrum method. The phase noise as a result of decorrelation can be significantly amplified when computing ionospheric phase using (2).

Decorrelation increases the chance of phase unwrapping errors. At C-band, the same amount of change due to displacement and troposphere, especially the stratification of the lower troposphere [50], corresponds to more fringes. This also increases the chance of phase unwrapping errors. In particular, the temporal decorrelation and stratified tropospheric phase are usually the dominant reasons causing phase unwrapping errors. The relative phase unwrapping errors between the lower and upper bands can be easily corrected by comparing the two unwrapped phases. However, the common phase unwrapping errors of the two bands are not easy to correct. The error in the computed ionospheric phase as a result of common phase unwrapping error is half of the common phase unwrapping error [15].

IV. IMPROVEMENT OF TIMES SERIES ANALYSIS AFTER IONOSPHERIC CORRECTION

A. Data

The Sentinel-1A/B satellites operate in a near-polar sun-synchronous (dawn-dusk) orbit at 693 km altitude. The repeat cycle is 12 days with each satellite, and is reduced to 6 days with the constellation. The ascending data are acquired around dusk, with a mean solar local time on ascending node (LTAN) of 18:00. The descending data are acquired around dawn. According to the temporal variations of the ionosphere, the ascending acquisitions are expected to be more severely affected by ionosphere. Considering also the spatial variations of the ionosphere, we select an ascending track and a descending track in western United States (mid-latitudes) and northern Chile (low-latitudes) to do the experiment. Both areas are characterized by large-scale tectonic motions.

The two tracks ascending 122 (A122) and descending 100 (D100) covering western United States are shown in Fig. 13. Since they are located at mid-latitudes, the TEC is not high even for track A122. The other two tracks ascending 149 (A149) and descending 156 (D156) covering northern Chile are shown in Fig. 14. We can see that the TEC for track A149 is very high. Each track has 4 slices with a time span of about 3.5 years. The numbers of acquisitions for each track are 52 (A122), 55 (D100), 62 (A149) and 59 (D156), respectively.

B. Processing

We form the sequential interferograms (only form interferograms with adjacent acquisitions) using the Sentinel-1 TOPS InSAR processor implemented in the JPL/Caltech ISCE software. When the data are acquired by Sentinel-1A and B alternately, this applies to each satellite individually in order to avoid the extra empirical ramp corrections in ionospheric correction. The newly implemented ionospheric correction module is used to do ionospheric correction. When the relative azimuth FM rate error between reference and repeat images is large enough to affect InSAR phase, we also correct for the resulting InSAR phase error. In the processing, ESD is applied whether doing ionospheric correction or not.

We use least squares to estimate the displacement time series which are then filtered by a temporal Gaussian filter. We estimate the mean velocity by fitting a linear polynomial to the filtered time series at each pixel. This is done for both interferogram stacks without and with ionospheric corrections.

The mean velocity from InSAR time series analysis is compared to that estimated from GPS time series downloaded from Nevada Geodetic Laboratory (http://geodesy.unr.edu/) by projecting the GPS velocity into the InSAR line-of-sight (LOS) direction. In areas near California, high-quality long-term GPS data are available. In other areas, only data of short time span are available for some stations. This affects the estimation of mean velocity, particularly when the displacement is non-linear. In addition, we find the inaccurate vertical velocity estimated from GPS data can significantly affect the root-mean-square (RMS) error in the comparison, especially for the two tracks in northern Chile. We therefore only project the two horizontal

GPS velocity components into InSAR LOS direction.

C. Results

The ionospheric correction results for the time series analysis are shown in Fig. 15 (western US, A122), Fig. 16 (western US, D100), Fig. 17 (northern Chile, A149) and Fig. 18 (northern Chile, D156), respectively.

The ionospheric effects in northern Chile (low-latitudes) are much stronger than those in western US (mid-latitudes), in agreement with the spatial variations of the Earth's ionosphere. Temporarily, the data acquired on ascending tracks (dusk) have much stronger ionospheric effects than those acquired on descending tracks (dawn), in agreement with the diurnal variations of the ionosphere. In the longer time scale, the ionospheric effect weakens from 2014 to 2018, which is governed by the 11-year solar cycle. To more clearly reveal the temporal variations associated with solar cycle, we compute the standard deviation of each ionospheric phase image and compare it with monthly mean total sunspot number in Fig. 19. The correlation between them for all four tracks is clear. However, no clear seasonal variations are found. Perhaps this is also because we don't have enough temporal sampling to reveal seasonal variations.

For the mean velocities estimated from time series analysis, the improvement after ionospheric corrections for track A149 in northern Chile is biggest as these data were acquired in low-latitudes around dusk. Ionospheric effect must be removed to measure the large-scale tectonic motion in this case. The improvement for tracks D156 in northern Chile and A122 in western US is small, but can still be clearly seen. Taking track A122 shown in Fig. 15 as an example, the colors inside the black circles at GPS stations CARE, AZRV and RG01 are closer to their surrounding colors with ionospheric correction, indicating the improvement brought by ionospheric correction. For these two tracks, ionospheric correction may be more important when exploring transient fault motion. For track D100 in western US, the RMS is slightly higher with ionospheric correction. This, however, is not surprising. First of all, the data were acquired at mid-latitudes around dawn, and therefore ionospheric effect is minimum, small enough to be ignored. Second, ionospheric correction contains not only improvement, but also errors. These errors can be from decorrelation, which is significantly amplified when computing ionospheric phase, and the common phase unwrapping errors of the lower and upper bands. In this case, ionospheric correction is not recommended.

In the results shown in Fig. 18, the RMS is higher than those of other tracks. In addition, Fig. 17 and Fig. 18 share some common GPS stations, but their values are different in the two figures. After inspecting the GPS data, we find that there are relatively large fluctuations due to unknown reasons (not seem to be seasonal). In addition, there are only short period of data available for some stations. As for InSAR data, the time spans of different tracks are not exactly the same. These reasons may contribute to the anomalies found in Fig. 17 and Fig. 18.

As we can see from Figs. 15-18, the ionospheric phase is mostly long-wavelength signal as already observed in previous

practice. Its effect in the mean velocity is also mostly long-wavelength signal, implying that a GPS network evenly distributed in the same area can be used to largely remove the effect. To further quantify its variations as a function of distance, we compute the following RMS along azimuth direction

$$\text{RMS}_{\text{azimuth}}(\Delta i) = \sqrt{\frac{\sum_{i=1}^{n_{\Delta i}} \left(\Delta\phi_{\text{ion}}^i - \Delta\phi_{\text{ion}}^{i+\Delta i} \right)^2}{n_{\Delta i}}} \qquad (20)$$

where $\Delta\phi_{\text{ion}}^i$ and $\Delta\phi_{\text{ion}}^{i+\Delta i}$ are two pixels with an azimuth separation or distance of Δi in the ionospheric phase image. Inside the square root, it means computing the difference squared of any pair of pixels separated by Δi, and taking the average. Inside the square root is actually the empirical variogram usually used in geostatistics which provides a description of how the data are correlated with distance. Here we don't include range direction due to the limitation of swath width. The number of samples available for the average in (20) decreases with separation or distance, therefore it is recommended the distance should not be larger than half of the image [51]. For our computation, we have a lot of columns in each image, and we use all the ionospheric phase images for each track, so we relax the limit to 0.8 image length. The results are shown in Fig. 20. Note that the result of track A149 is divided by 5 in order to fit into the plot. We can see that even within a distance of more than 500 km, $\text{RMS}_{\text{azimuth}}(\Delta i)$ is still mostly linearly increasing with distance, with no indication of decreasing or approaching a maximum value (or sill as called in variogram terminology). This provides an idea of the impact of the ionospheric effect in terms of scale.

V. CONCLUSION

Overall, the range split-spectrum method is effective and successful in removing the phase introduced by ionospheric effects for C-band Sentinel-1 TOPS mode InSAR data. Extra-corrections are required when computing ionospheric phase for pairs with different starting ranges and cross Sentinel-1A/B pairs. Very accurate correction, especially near burst edges, is limited by the requirement of the height of the ionosphere and the need for strongly filtering the computed ionospheric phase considering the relatively small separation of the two range subbands. The major limitations of this method for operational use are decorrelation and phase unwrapping error, which are more severe at C-band.

The behaviors of the ionosphere are already studied in a number of other related fields, which is important for looking at the ionospheric effects in InSAR. By processing four representative Sentinel-1 InSAR stacks acquired at different latitudes and different local times of a day (or orbit directions), we find that the ionospheric effects are very strong for data acquired at low-latitudes (geomagnetic latitude) on ascending tracks (dusk-side of the Sentinel-1 dawn-dusk orbit). The introduced phase must be removed in order to get usable results from time series analysis. For data acquired at low-latitudes on descending tracks (dawn-side of the Sentinel-1 dawn-dusk orbit) and at mid-latitudes on ascending tracks, the ionospheric effects are small, but improvement after correction is still clear in the time series analysis results. In these cases, ionospheric

correction may be more important when exploring transient fault motion. For data acquired at mid-latitudes on descending tracks, ionospheric effects are mostly small enough to be ignored, and corrections are therefore not recommended. The errors introduced by ionosphere are mostly long-wavelength signals, and therefore ionospheric correction can be important for measuring large-scale tectonic motion.

REFERENCES

[1] Y. Bock and D. Melgar, "Physical applications of GPS geodesy: A review," *Rep. Prog. Phys.*, vol. 79, no. 10, pp. 1-119, Aug. 2016.
[2] D. Geudtner, R. Torres, P. Snoeij, M. Davidson, and B. Rommen, "Sentinel-1 system capabilities and applications," in *Proc. IEEE IGARSS*, Quebec City, QC, Canada, Jul. 2014, pp. 1457-1460.
[3] P. Snoeij, R. Torres, D. Geudtner, M. Brown, P. Deghaye, I. Navas-Traver, A. Østergaard, B. Rommen, N. Floury, and M. Davidson, "Sentinel-1 instrument overview," presented at *SEASAR 2012*, Tromsø, Norway, Jun. 2012.
[4] https://earth.esa.int/web/eoportal/satellite-missions/c-missions/copernicus-sentinel-1
[5] F. De Zan and A. Monti Guarnieri, "TOPSAR: Terrain observation by progressive scans," *IEEE Trans. Geosci. Remote Sens.*, vol. 44, no. 9, pp. 2352-2360, Sep. 2006.
[6] P. Prats-Iraola, R. Scheiber, L. Marotti, S. Wollstadt, and A. Reigber, "TOPS interferometry with TerraSAR-X," *IEEE Trans. Geosci. Remote Sens.*, vol. 50, no. 8, pp. 3179-3188, Aug. 2012.
[7] A. L. Gray, K. E. Mattar, and G. Sofko, "Influence of ionospheric electron density fluctuations on satellite radar interferometry," *Geophys. Res. Lett.*, vol. 27, no. 10, pp. 1451-1454, May. 2000.
[8] I. Joughin, D. Winebrenner, M. Fahnestock, R. Kwok, and W. Krabill, "Measurement of ice-sheet topography using satellite-radar interferometry," *J. Glac.*, vol. 42, no. 140, pp. 10-22, 1996.
[9] M.-H. Huang, H. Tung, E. J. Fielding, H.-H. Huang, C. Liang, C. Huang, and J.-C. Hu, "Multiple fault slip triggered above the 2016 Mw 6.4 MeiNong earthquake in Taiwan," *Geophys. Res. Lett.*, vol. 43, no. 14, pp. 7459-7467, Jul. 2016.
[10] H. Fattahi, P. Agram, and M. Simons, "A network-based enhanced spectral diversity approach for TOPS time-series analysis," *IEEE Trans. Geosci. Remote Sens.*, vol. 55, no. 2, pp. 777-786, Feb. 2017.
[11] K. Wang, X. Xu, and Y. Fialko, "Improving burst alignment in TOPS interferometry with bivariate enhanced spectral diversity," *IEEE Geosci. Remote Sens. Lett.*, vol. 14, no. 12, pp. 2423-2427, Dec. 2017.
[12] P. A. Rosen, S. Hensley, and C. Chen, "Measurement and mitigation of the ionosphere in L-band interferometric SAR data," in *Proc. IEEE Radar Conf.*, Washington, DC, USA, May 2010, pp. 1459-1463.
[13] R. Brcic, A. Parizzi, M. Eineder, R. Bamler, and F. Meyer, "Estimation and compensation of ionospheric delay for SAR interferometry," in *Proc. IEEE IGARSS*, Honolulu, HI, USA, Jul. 2010, pp. 2908-2911.
[14] F. J. Meyer, P. Rosen, A. Freeman, K. Papathanassiou, J. Nicoll, B. Watkins, M. Eineder, R. Bricic, and T. Ainsworth, "A review of ionospheric effects in low-frequency SAR data signals," presented at *Proc. IEEE IGARSS*, Honolulu, HI, USA, Jul. 2010.
[15] G. Gomba, A. Parizzi, F. de Zan, M. Eineder, and R. Bamler, "Toward operational compensation of ionospheric effects in SAR interferograms: The split-spectrum method," *IEEE Trans. Geosci. Remote Sens.*, vol. 54, no. 3, pp. 1446-1461, Mar. 2016.
[16] H. Fattahi, M. Simons, and P. Agram, "InSAR time-series estimation of the ionospheric phase delay: An extension of the split range-spectrum technique," *IEEE Trans. Geosci. Remote Sens.*, vol. 55, no. 10, pp. 5984-5996, Jul. 2017.
[17] H. Liao, F. J. Meyer, B. Scheuchl, J. Mouginot, I. Joughin, and Eric Rignot, "Ionospheric correction of InSAR data for accurate ice velocity measurement at polar regions," *Remote Sens. Environ.*, vol. 209, pp. 166-180, May 2018.
[18] C. Liang and E. J. Fielding, "Measuring azimuth deformation with L-band ALOS-2 ScanSAR interferometry," *IEEE Trans. Geosci. Remote Sens.*, vol. 55, no. 5, pp. 2725-2738, May 2017.
[19] G. Gomba, F. R. González, and F. De Zan, "Ionospheric phase screen compensation for the Sentinel-1 TOPS and ALOS-2 ScanSAR modes," *IEEE Trans. Geosci. Remote Sens.*, vol. 55, no. 1, pp. 223-235, Jan. 2017.
[20] IEEE Standard Definitions of Terms for Radio Wave Propagation, IEEE Standard 211, 1997.
[21] M. B. McElroy, "Ionosphere and magnetosphere," ENCYCLOPÆDIA BRITANNICA. [Online]. Available: https://www.britannica.com/science/ionosphere-and-magnetosphere
[22] D. L. Wu, C. O. Ao, G. A. Hajj, M. de la Torre Juarez, and A. J. Mannucci, "Sporadic E morphology from GPS-CHAMP radio occultation," *J. Geophys. Res.*, vol. 110, no. A1, pp. 1-18, Jan. 2005.
[23] W. Swider, *Aerospace environment*, Air Force Geophysics Laboratory, United States Air Force, Hanscom AFB, MA, USA.
[24] World Data Center for Geomagnetism, Kyoto. http://wdc.kugi.kyoto-u.ac.jp/
[25] K.-H. Glaßmeier H. Soffel, and J. Negendank (Eds.), *Geomagnetic Field Variations*. Springer-Verlag Berlin Heidelberg 2009, pp. 53-54.
[26] B. Zolesi and L. R. Cander, *Ionospheric Prediction and Forecasting*. Springer-Verlag Berlin Heidelberg 2014.
[27] M. Hernández-Pajares, J. M. Juan, J. Sanz, R. Orus, A. Garcia-Rigo, J. Feltens, A. Komjathy, S. C. Schaer, and A. Krankowski, "The IGS VTEC maps: A reliable source of ionospheric information since 1998," *J. Geod.*, vol. 83, no. 3-4, pp. 263-275, Mar. 2009.
[28] E. V. Appleton, "Two anomalies in the ionosphere," *Nature*, vol. 157, no. 3995, pp. 691, May. 1946.
[29] X. Pi, A. Freeman, B. Chapman, P. Rosen, and Z. Li, "Imaging ionospheric inhomogeneities using spaceborne synthetic aperture radar," *J. Geophys. Res.*, vol. 116, no. A4, pp. 1-13, Apr. 2011.
[30] X. Pi, "Ionospheric effects on spaceborne synthetic aperture radar and a new capability of imaging the ionosphere from space," *Space Weather*, vol. 13, no. 11, pp. 737-741, Nov. 2015.
[31] F. J. Meyer, K. Chotoo, S. D. Chotoo, B. D. Huxtable, and C. S. Carrano, "The influence of equatorial scintillation on L-band SAR image quality and phase," *IEEE Trans. Geosci. Remote Sens.*, vol. 54, no. 2, pp. 869-880, Feb. 2016.
[32] R. D. Hunsucker and J. K. Hargreaves, *The High-Latitude Ionosphere and its Effects on Radio Propagation*. Cambridge, United Kingdom: Cambridge University Press, 2009.
[33] I. Joughin, B. E. Smith, I. M. Howat, T. Scambos, and T. Moon, "Greenland flow variability from ice-sheet-wide velocity mapping," *J. Glac.*, vol. 56, no. 197, pp. 415-430, 2010.
[34] *Handbook of Geophysics and the Space Environment*, 4th ed., Air Force Geophysics Laboratory, United States Air Force, Hanscom AFB, MA, USA, 1985, pp. 9-4.
[35] D. H. Hathaway, "The solar cycle," *Living Rev. Solar Phys.*, vol. 12, no. 1, pp. 1-87, Dec. 2015.
[36] F. Meyer, "A review of ionospheric effects in low-frequency SAR - Signals, correction methods, and performance requirements," in *Proc. IEEE IGARSS*, Honolulu, HI, USA, Jul. 2010, pp. 2908-2911.
[37] F. Meyer, R. Bamler, N. Jakowski, and T. Fritz, "The potential of low-frequency SAR systems for mapping ionospheric TEC distributions," *IEEE Geosci. Remote Sens. Lett.*, vol. 3, no. 4, pp. 560-564, Oct. 2006.
[38] F. J. Meyer, "Performance requirements for ionospheric correction of low-frequency SAR data," *IEEE Trans. Geosci. Remote Sens.*, vol. 49, no. 10, pp. 3694-3702, Oct. 2011.
[39] R. Scheiber and A. Moreira, "Coregistration of interferometric SAR images using spectral diversity," *IEEE Trans. Geosci. Remote Sens.*, vol. 38, no. 5, pp. 2179-2191, Sep. 2000.
[40] E. Sansosti, P. Berardino, M. Manunta, F. Serafino, and G. Fornaro, "Geometrical SAR image registration," *IEEE Trans. Geosci. Remote Sens.*, vol. 44, no. 10, pp. 2861-2870, Oct. 2006.
[41] C. W. Chen, and H. A. Zebker, "Two-dimensional phase unwrapping with use of statistical models for cost functions in nonlinear optimization," *J. Opt. Soc. Am. A*, vol. 18, no. 2, pp. 338-351, Feb. 2001.
[42] L. M. H. Ulander and J. Askne, "Repeat-pass SAR interferometry over forested terrain," *IEEE Trans. Geosci. Remote Sens.*, vol. 33, no. 2, pp. 331-340, Mar. 1995.
[43] C. Liang, E. J. Fielding, and M.-H. Huang, "Estimating azimuth offset with double-difference interferometric phase: The effect of azimuth FM rate error in focusing," *IEEE Trans. Geosci. Remote Sens.*, vol. 55, no. 12, pp. 7018-7031, Dec. 2017.

[44] M. Schwerdt, K. Schmidt, N. T. Ramon, P Klenk, N. Yague-Martinez, P. Prats-Iraola, M. Zink, and D. Geudtner, "Independent System Calibration of Sentinel-1B," *Remote Sens.*, vol. 9, no. 6, pp. 1-34, Jun. 2017.

[45] F. Gatelli, A. Monti Guarnieri, F. Parizzi, P. Pasquali, C. Prati, and F. Rocca, "The wavenumber shift in SAR interferometry," *IEEE Trans. Geosci. Remote Sensing*, vol. 32, no. 4, pp. 855-865, Jul. 1994.

[46] H. A. Zebker, and J. Villasenor, "Decorrelation in interferometric radar echoes," *IEEE Trans. Geosci. Remote Sens.*, vol. 30, no. 5, pp. 950-959, Sep. 1992.

[47] E. W. Hoen and H. A. Zebker, "Penetration depths inferred from interferometric volume decorrelation observed over the Greenland ice sheet," *IEEE Trans. Geosci. Remote Sens.*, vol. 38, no. 6, pp. 2571-2583, Nov. 2000.

[48] A. Monti Guarnieri and F. Rocca, "Combination of low- and high-resolution SAR images for differential interferometry," *IEEE Trans. Geosci. Remote Sens.*, vol. 37, no. 4, pp. 2035-2049, Jul. 1999.

[49] M. Martone, P. Rizzoli, and G. Krieger, "Volume decorrelation effects in TanDEM-X interferometric SAR data," *IEEE Geosci. Remote Sens. Lett.*, vol. 13, no. 12, pp. 1812-1816, Dec. 2016.

[50] R. Jolivet, P. S. Agram, N. Y. Lin, M. Simons, M.-P. Doin, G. Peltzer, and Z. Li, "Improving InSAR geodesy using Global Atmospheric Models," *J. Geophys. Res.*, vol. 119, no. 3, pp. 2324-2341, Mar. 2014.

[51] R. A. Olea, "A practical primer on geostatistics," U.S. Geological Survey, Reston, VA, USA, Open-File Report 2009-1103, 2009.

[52] P. Wessel, W. H. F. Smith, R. Scharroo, J. Luis, and F. Wobbe, "Generic mapping tools: Improved version released," *EOS Trans. AGU*, vol. 94, no. 45, pp. 409-410, 2013.
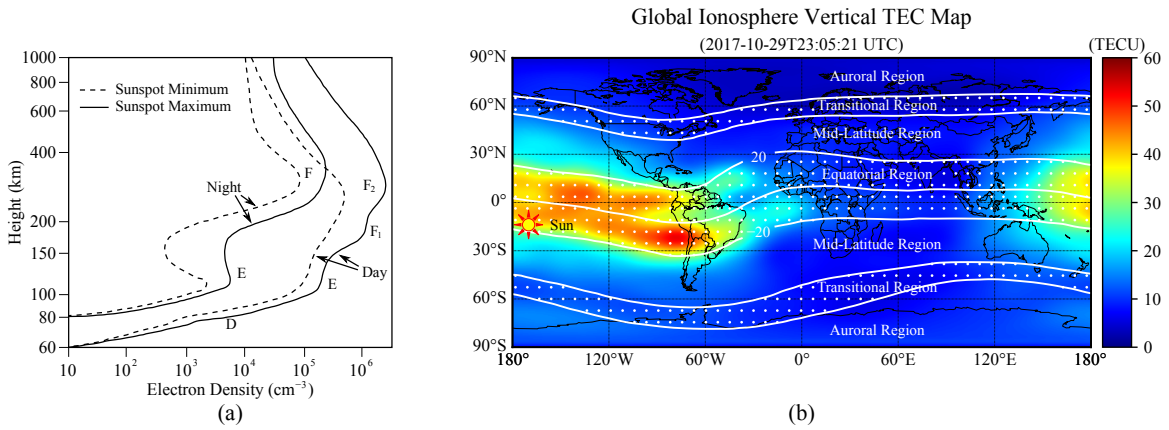
Fig. 1. (a) Typical vertical profiles of electron density in the mid-latitude ionosphere [23]. (b) Ionospheric regions according to their *geomagnetic latitudes* [26] overlaid on a global vertical TEC map interpolated from results processed by NASA JPL (https://iono.jpl.nasa.gov/) using data from International GNSS Service.
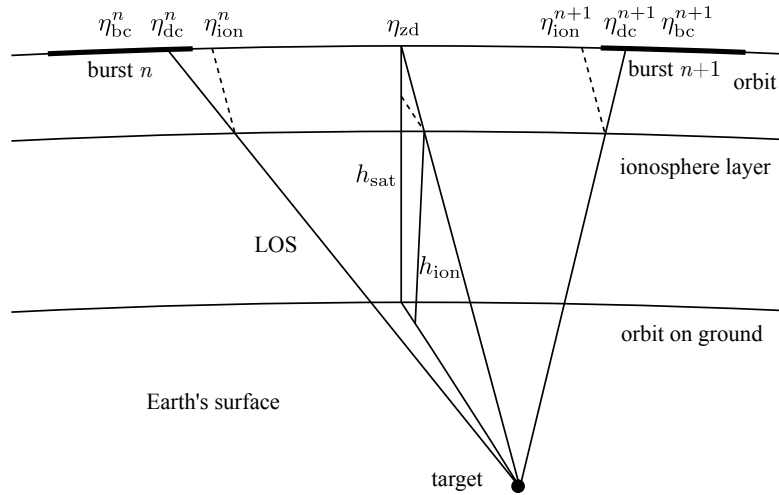
Fig. 2. The imaging geometry of Sentinel-1 TOPS mode considering the ionosphere simplified as a layer.

reference and repeat bursts   offset

removing window and bandpass filtering to
generate lower and upper band bursts

resampling repeat bursts to form subband
burst interferograms

different starting
ranges or
combination of   yes
Sentinel-1A/B?
                    no

computing burst mosaicking edges according   computing burst mosaicking edges according
to the number of looks   to the number of looks

mosaicking and multiple looking all bursts of   mosaicking and multiple looking all bursts of
all subswaths at each subband   *each* subswath at each subband

unwrapping subband interferograms   unwrapping subband interferograms

computing ionospheric phase   computing ionospheric phase

                                                     mosaicking subswaths

                                                     combination of
                                            no   Sentinel-1A/B?
                                                 yes

                                                     compensating range ramp

projecting ionospheric phase from ground
onto ionosphere layer

filtering ionospheric phase   →   computing azimuth shift caused by
                                              ionosphere

projecting ionospheric phase from   computing phase error caused by ionosphere
ionosphere layer onto ground   azimuth shift

adding ionospheric phase and phase error
caused by ionosphere azimuth shift

ESD to estimate residual azimuth offset and   reference and resampled
computing the resulting phase error   repeat bursts

adding ionospheric phase, phase error caused by ionosphere
azimuth shift, and phase error caused by residual offset

burst-level phase for doing correction

Fig. 3. The overall workflow for the InSAR ionospheric correction of Sentinel-1 TOPS mode.
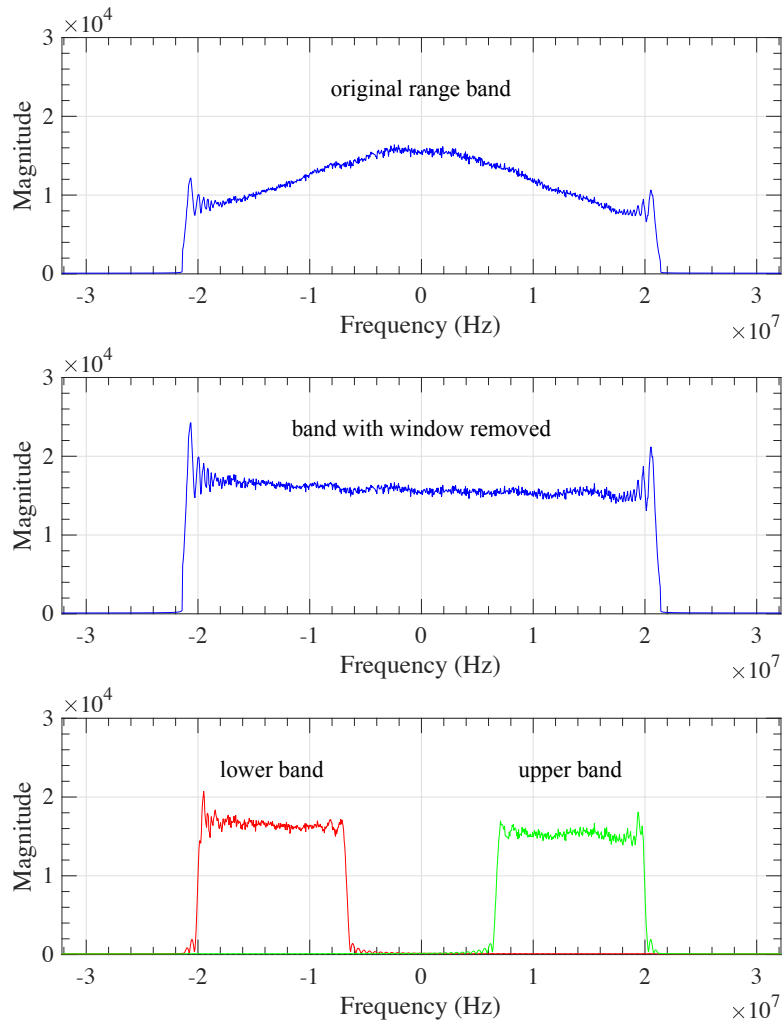
Fig. 4. The bandpass filtering process for a burst.
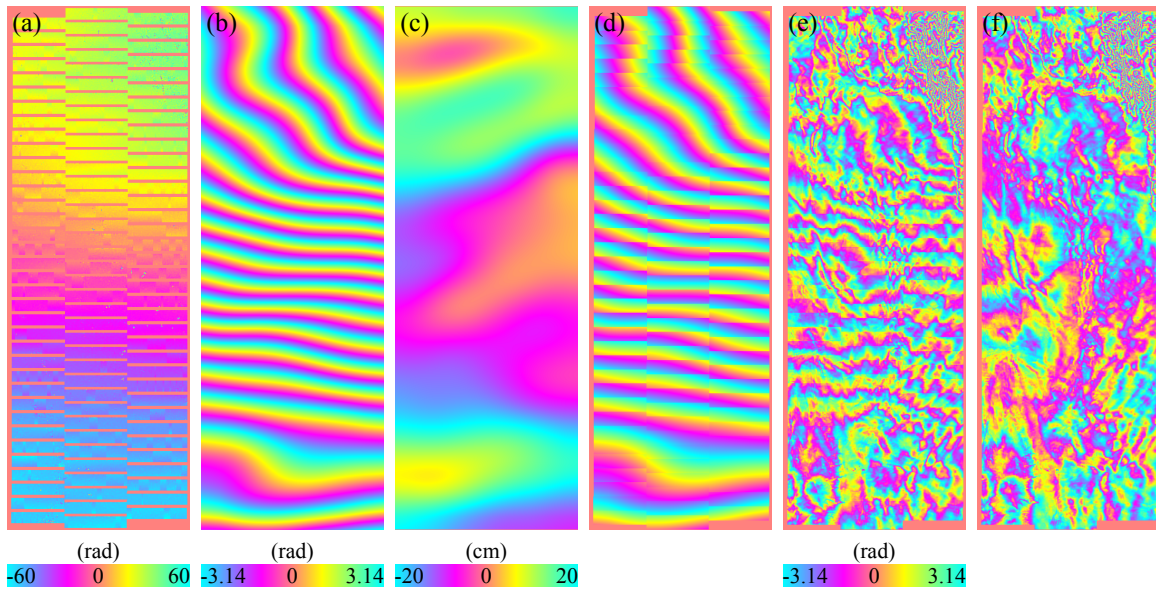
Fig. 5. InSAR ionospheric correction for Sentinel-1 TOPS mode. (a) Ionospheric phase at the ionosphere layer. (b) Filtered ionospheric phase at the ionosphere layer. (c) Azimuth shift caused by ionosphere. (d) Phase for correction. (e) Original interferogram with ESD applied. (f) Corrected interferogram. Note that the values in (a)-(d) are wrapped. The data partly cover northern Chile with a size of 250km×690km (range×azimuth) and were acquired on October 29, 2017 and November 10, 2017 on ascending track 149.
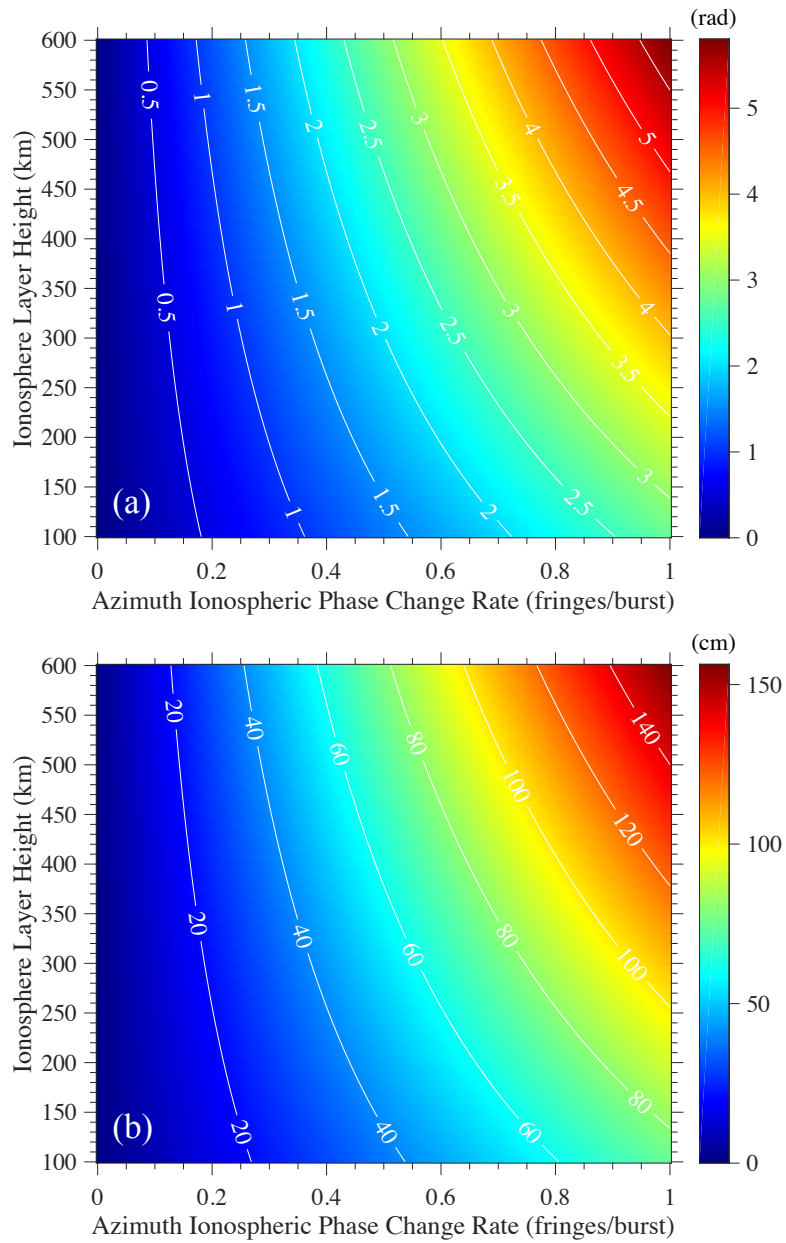
Fig. 6. (a) The phase discontinuity caused by ionosphere in the burst overlap area. (b) The equivalent azimuth offset in ESD. The offset is measured on ground.
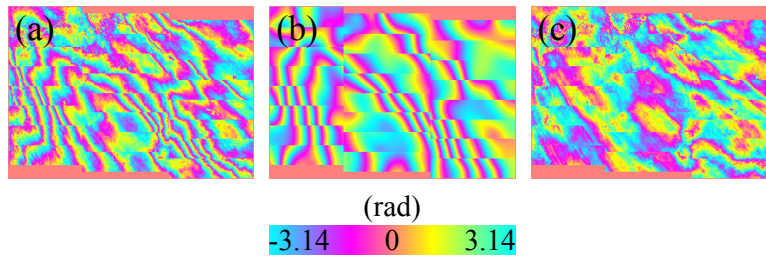
Fig. 7. Ionospheric correction for interferogram with high frequency ionospheric effects. (a) Original interferogram. (b) Phase for correction. (c) Corrected interferogram. The data cover Mexico City, Mexico and were acquired on December 9, 2015 and December 21, 2015 on descending track 143.
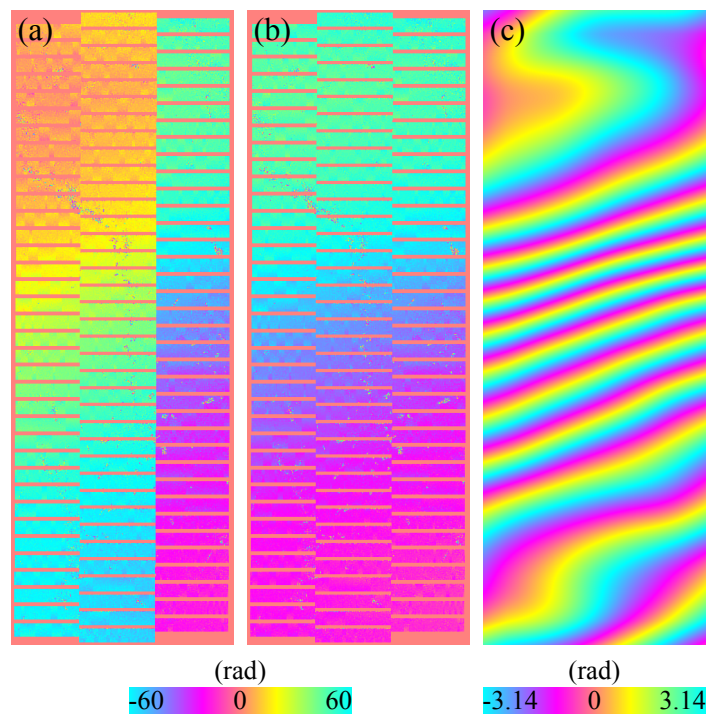
Fig. 8. Computed ionospheric phase for a pair with different starting ranges. (a) Original computed ionospheric phase. (b) Ionospheric phase after removing discontinuities between subswaths. (c) Ionospheric phase after filtering. The data partly cover northern Chile and were acquired on April 13, 2015 and May 7, 2015 on ascending track 149.
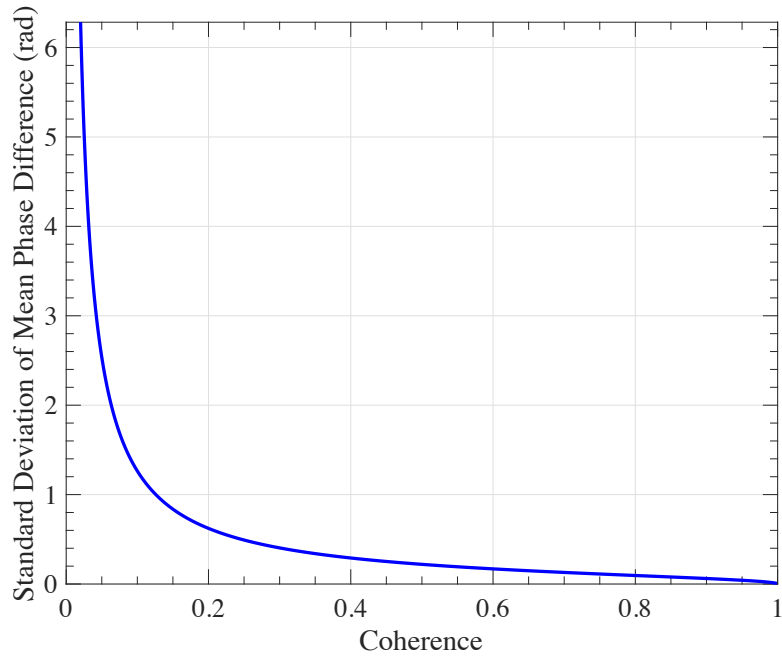
Fig. 9. The standard deviation of the mean subswath ionospheric phase difference of one slice as a result of decorrelation.

(rad)

-3.14   0   3.14
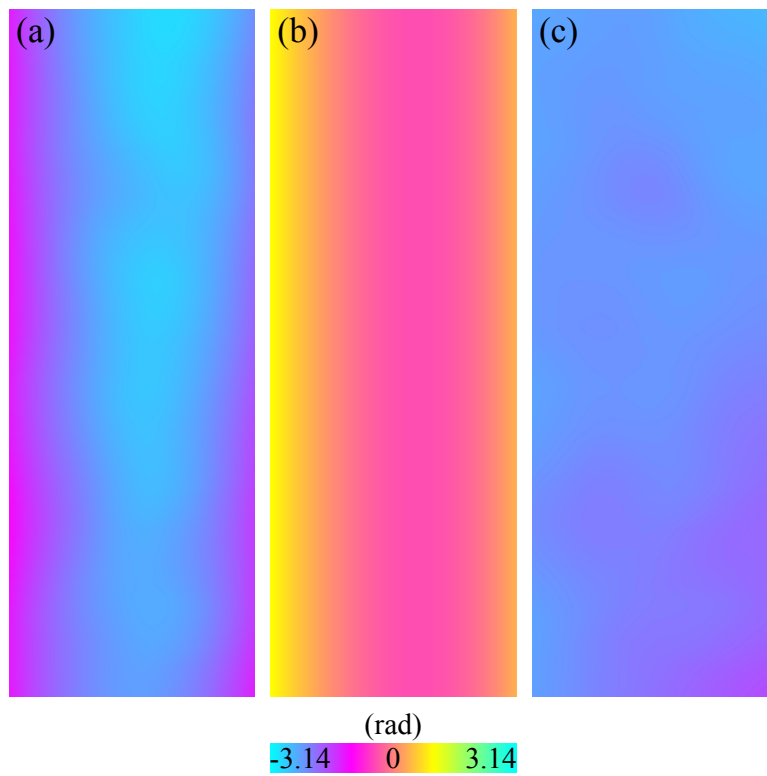
Fig. 10. Range ramp in the computed ionospheric phase of a cross Sentinel-1A/B pair. (a) Original ionospheric phase. (b) Range ramp. (c) Ionospheric phase after removing range ramp. The data partly cover northern Chile and were acquired on July 25, 2016 (Sentinel-1A) and September 29, 2016 (Sentinel-1B) on descending track 156.
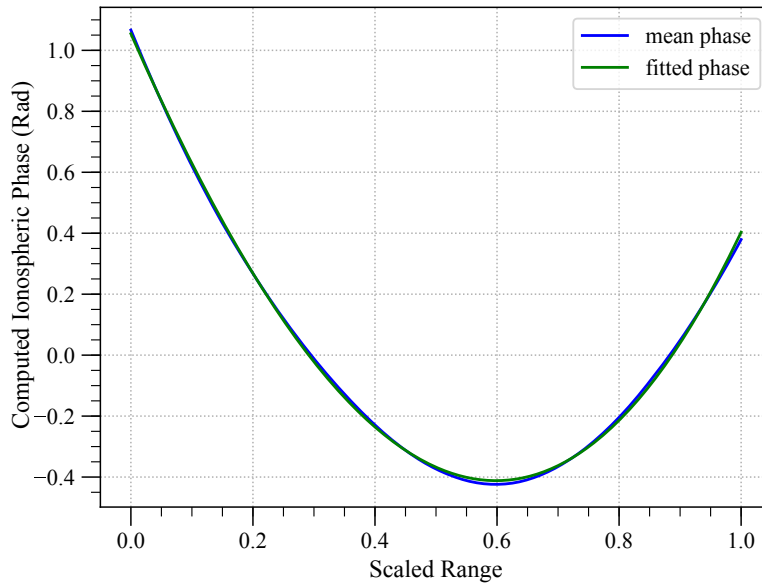
Fig. 11. The range ramp estimated from computed ionospheric phase of the pair shown in Fig. 10.
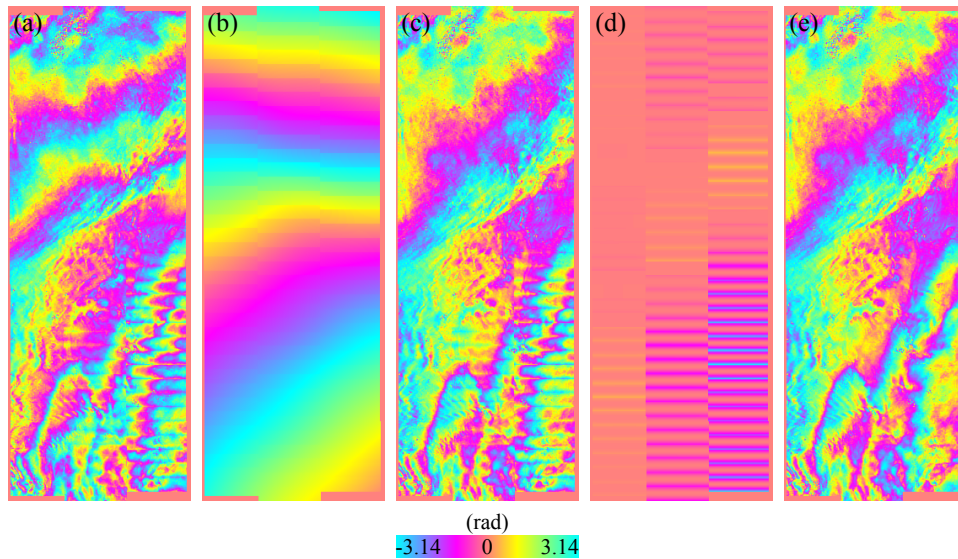
Fig. 12. (a) Original interferogram. (b) Ionospheric phase. (c) Interferogram with only ionospheric correction. (d) Phase error caused by relative azimuth FM rate error. (e) Interferogram with both ionospheric correction and correction for relative azimuth FM rate error. The data partly cover northern Chile and were acquired on November 4, 2015 (focused by IPF 002.53) and November 28, 2015 (focused by IPF 002.60) on descending track 156.
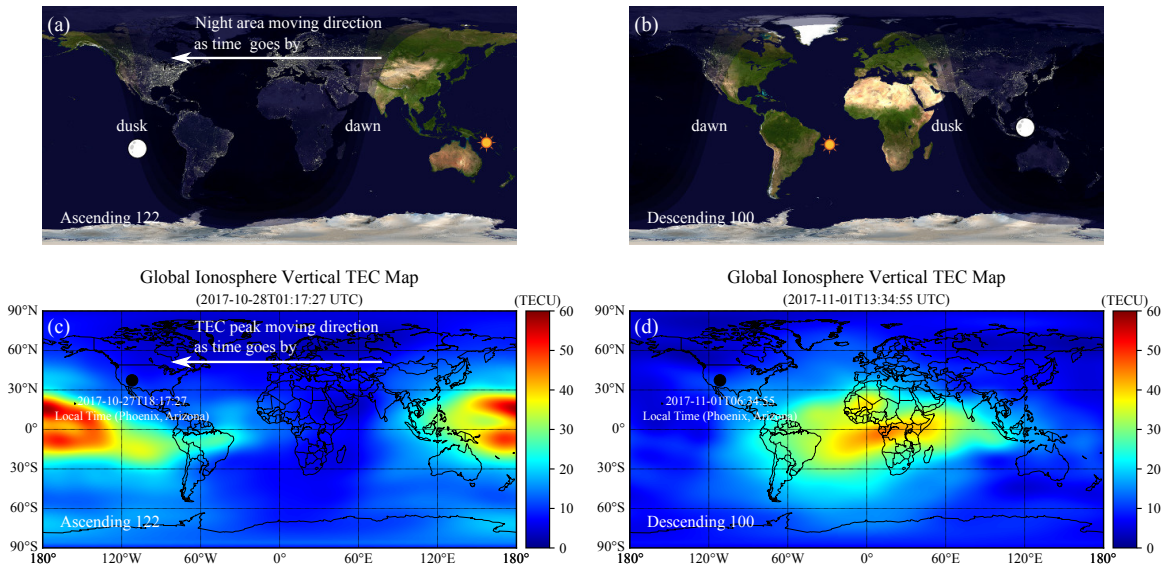
Fig. 13. The two tracks covering western US (mid-latitudes). (a) and (b) are the global day and night maps at the time when the data were acquired (Courtesy of https://www.timeanddate.com). (c) and (d) are the corresponding global vertical TEC maps. The black dots in (c) and (d) denote the imaged areas by the two tracks.
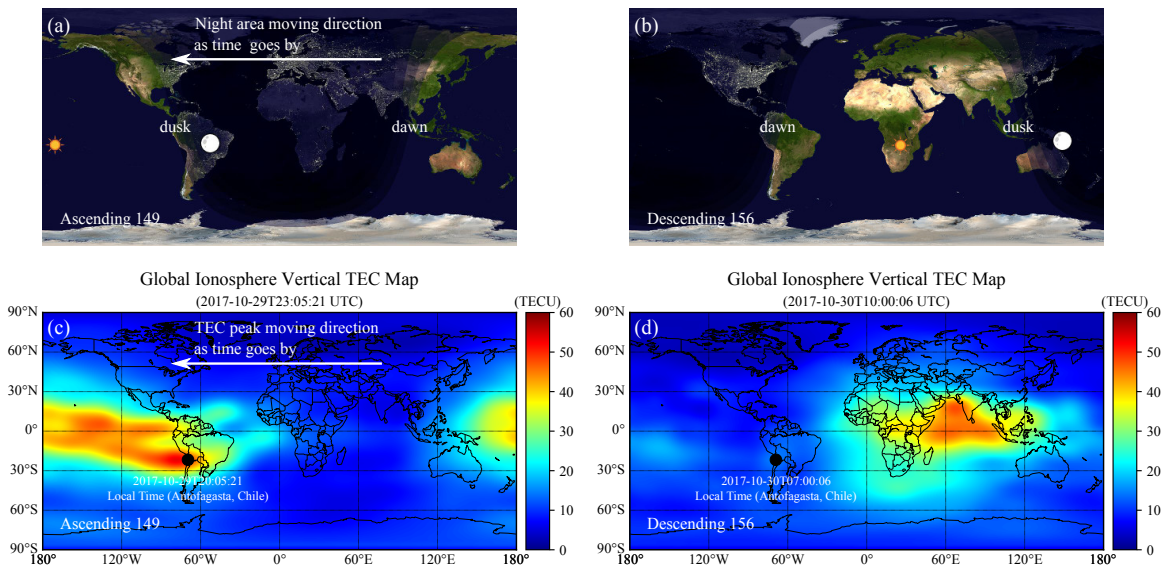
Fig. 14. Same as Fig. 13, but for the two tracks covering northern Chile (low-latitudes).
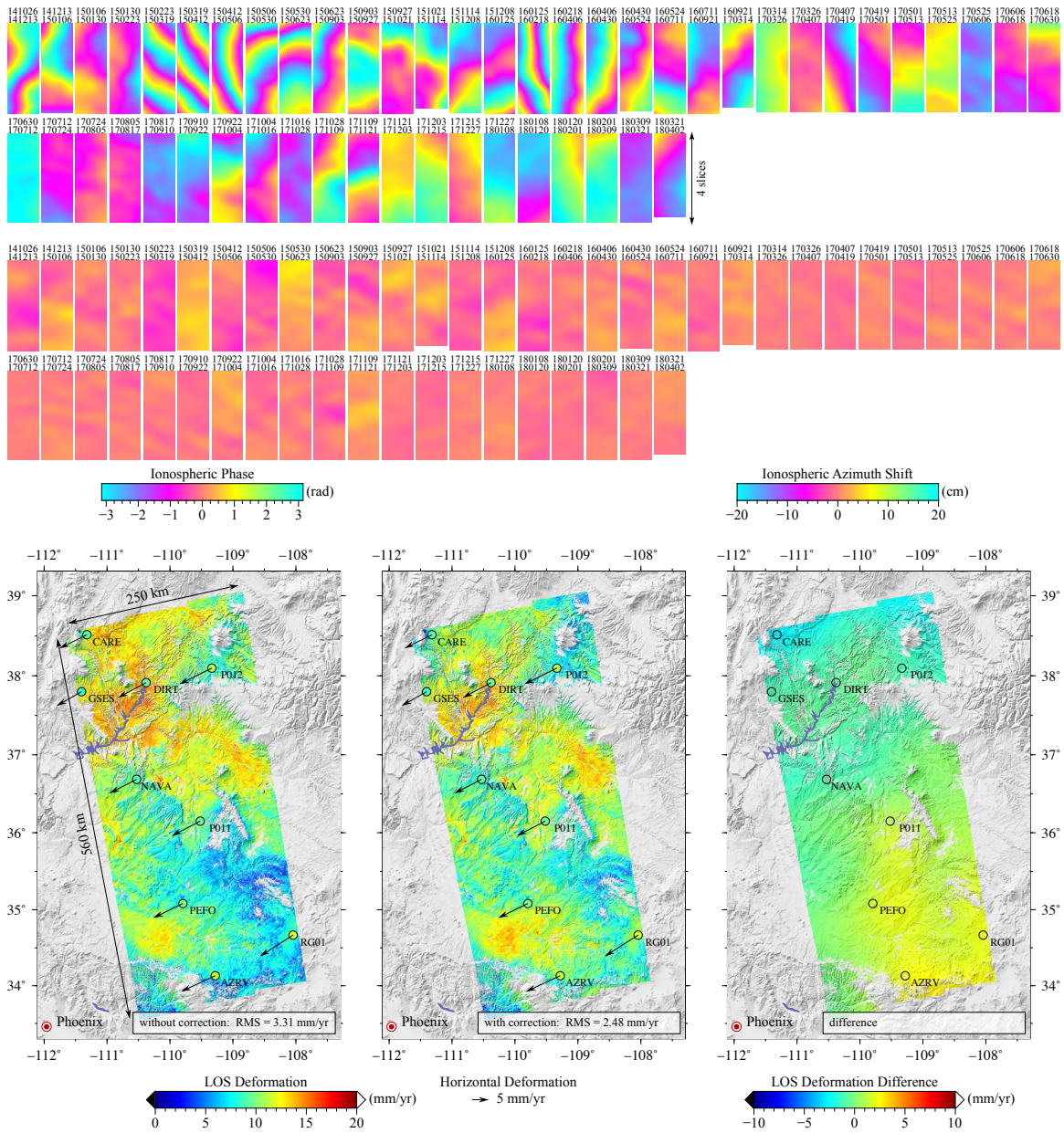
Fig. 15. Ionospheric correction results of track A122 in western US (mid-latitudes). Top: computed ionospheric phase for each interferogram. Middle: computed azimuth shift caused by ionosphere for each interferogram. Bottom: estimated mean velocities. In the bottom panels, the black circles denote GPS stations with station names to the lower right. The arrows and the colors in the circles in the first two panels denote GPS horizontal velocities, and the GPS velocities projected into InSAR LOS directions.
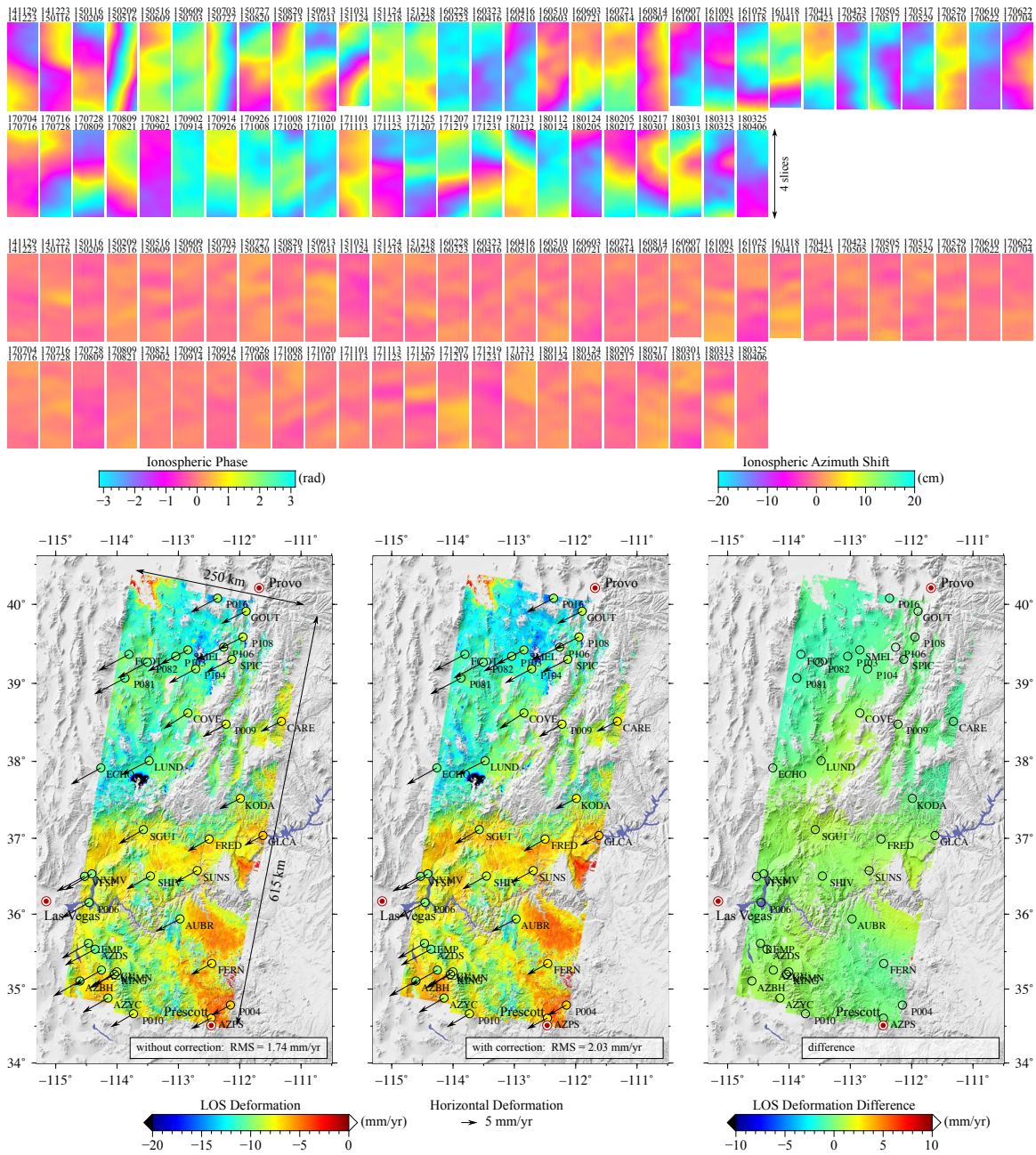
Fig. 16. Same as Fig. 15. Track D100 in western US (mid-latitudes).
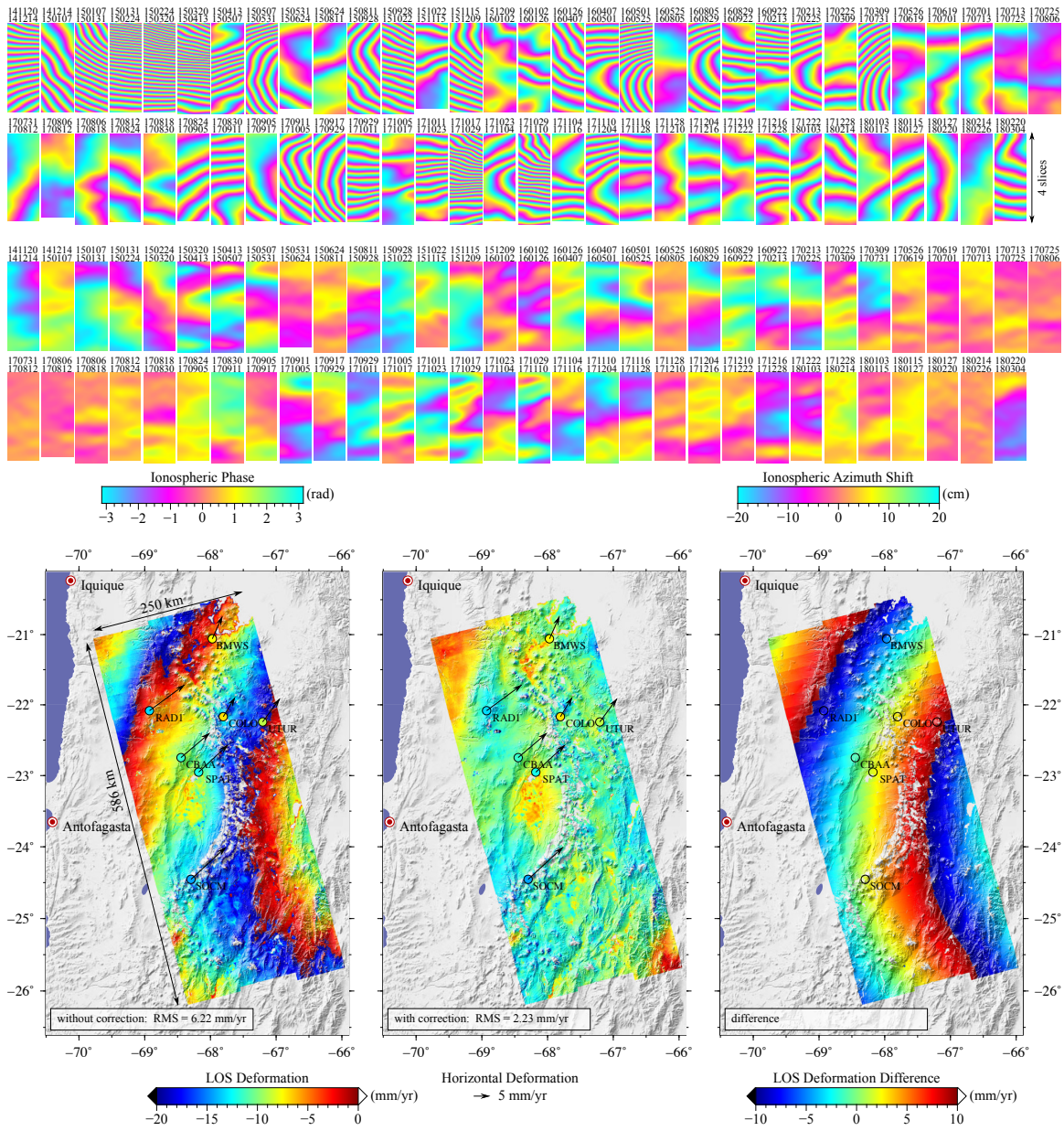
Fig. 17. Same as Fig. 15. Track A149 in northern Chile (low-latitudes). Note that the data in the first and third panels at bottom are wrapped before plotting.
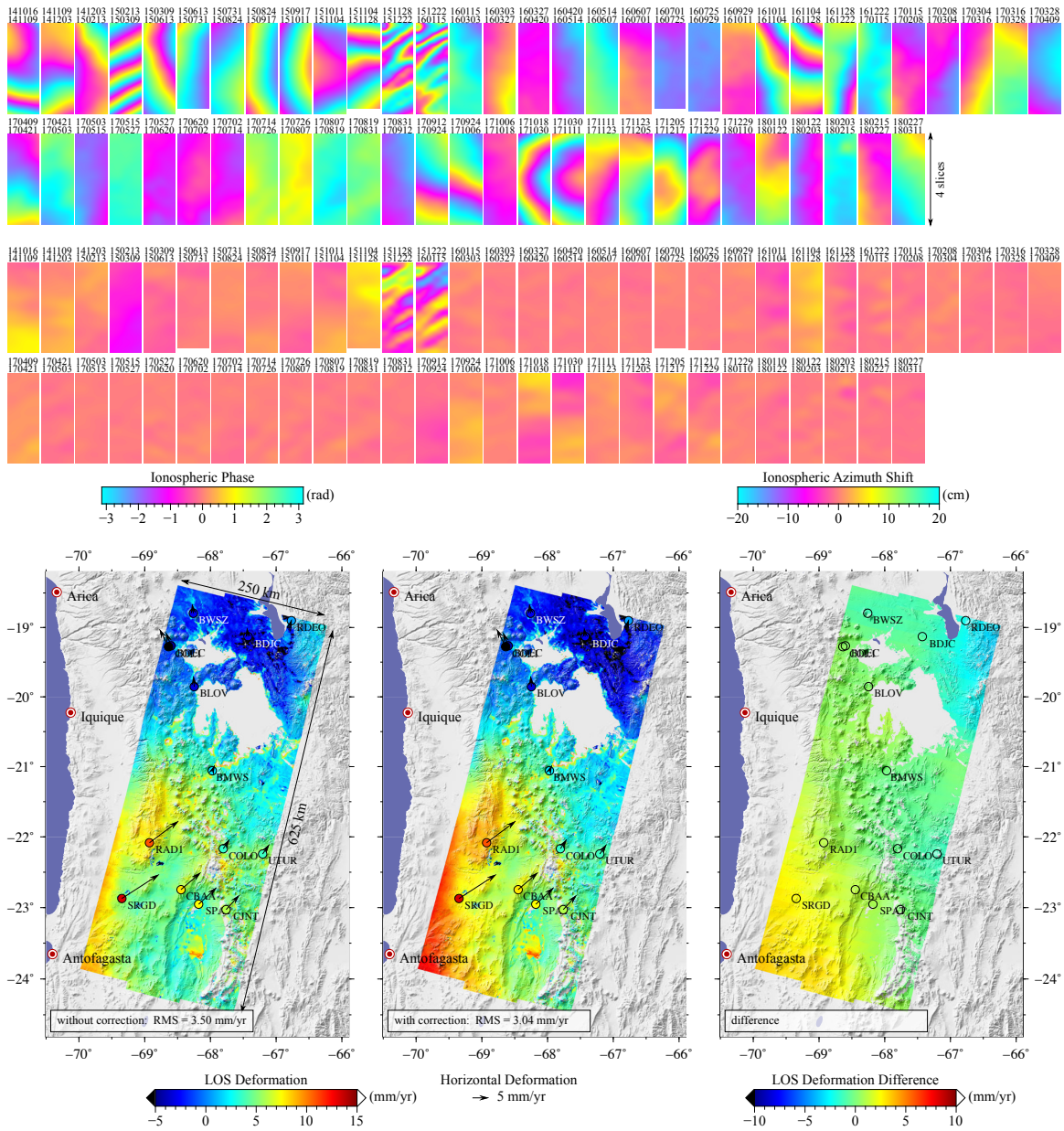
Fig. 18. Same as Fig. 15. Track D156 in northern Chile (low-latitudes).
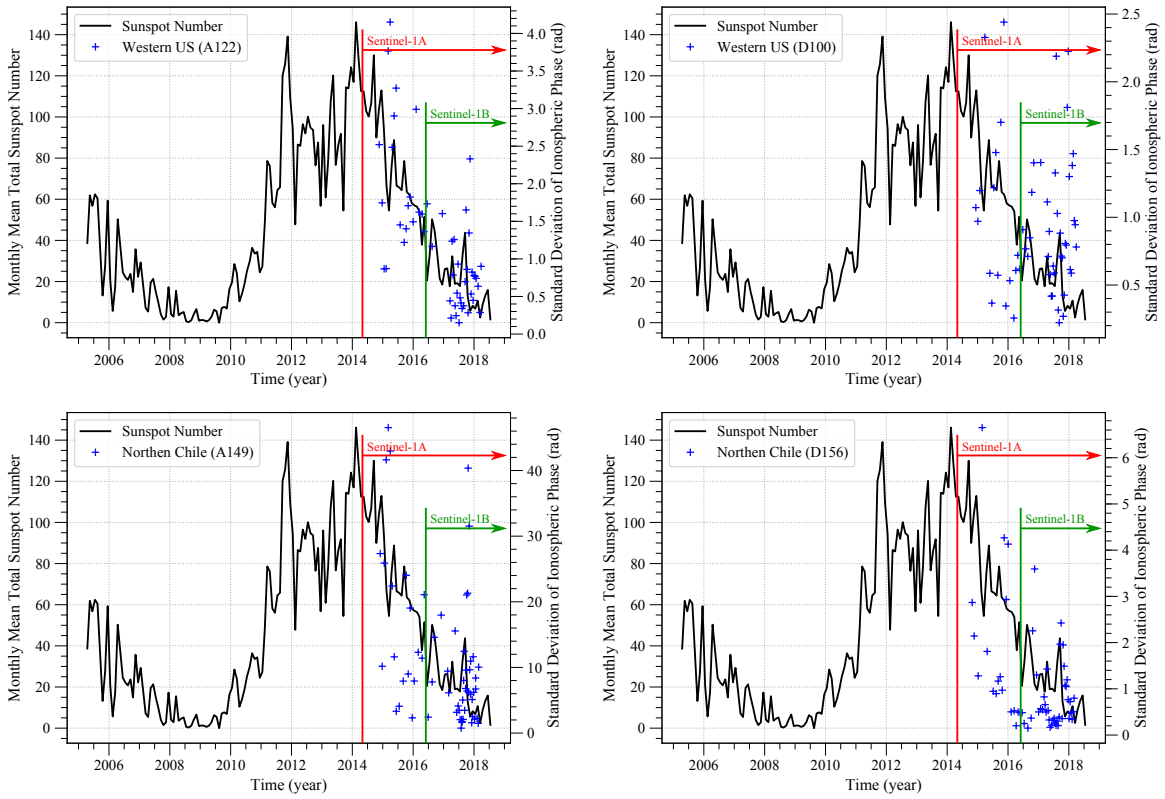
Fig. 19. The correlation between the solar activity (sunspot number) and the ionospheric effect (ionospheric phase). The sunspot number is from WDC-SILSO, Royal Observatory of Belgium, Brussels, Belgium.
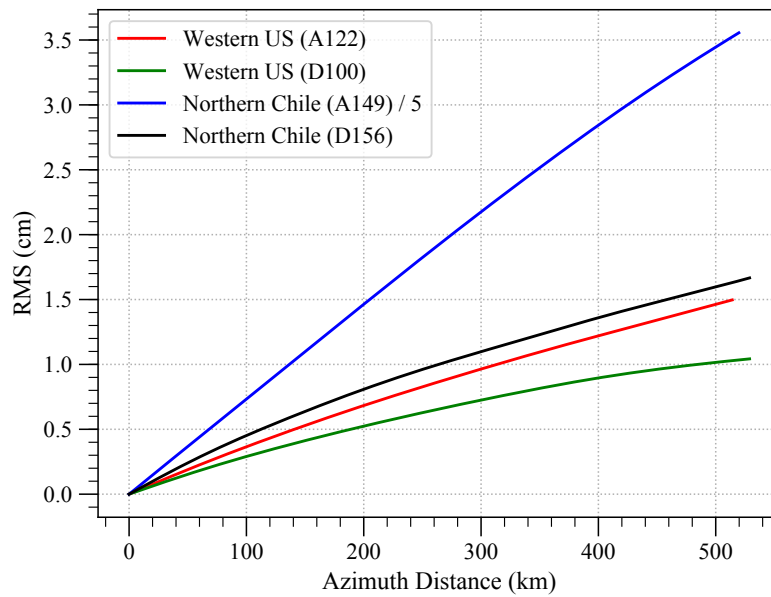

Fig. 20. The variation of ionospheric phase (converted to deformation) as a function of azimuth distance.